arXiv:1604.08544v1 [math.NA] 28 Apr 2016

NUMERICAL METHODS FOR INTERFACE COUPLING OF COMPRESSIBLE AND ALMOST INCOMPRESSIBLE MEDIA. *

M. J. DEL RAZO† AND R. J. LEVEQUE †

Abstract. Many experiments in biomedical applications and other disciplines use a shock tube. These experiments often involve placing an experimental sample within a fluid-filled container, which is then placed inside the shock tube. The shock tube produces an initial shock that propagates through gas before hitting the container with the sample. In order to gain insight into the shock dynamics that is hard to obtain by experimental means, computational simulations of the shock wave passing from gas into a thin elastic solid and into a nearly incompressible fluid are developed. It is shown that if the solid interface is very thin, it can be neglected, simplifying the model. The model uses Euler equations for compressible fluids coupled with a Tammann equation of state (EOS) to model both compressible gas and almost incompressible materials. A three-dimensional (2D axisymmetric) model of these equations is solved using high-resolution shock-capturing methods, with newly developed Riemann solvers and limiters. The methods are extended to work on a mapped grid to allow more complicated interface geometry, and they are adapted to work with adaptive mesh refinement (AMR) for higher resolution and faster computations. The Clawpack software is used to implement the method. These methods were initially inspired by shock tube experiments to study the injury mechanisms of traumatic brain injury (TBI).

Key words. Euler equations, Tammann equation of state, compressible and almost incompressible fluid interfaces, finite volume methods, mapped grids, shock tube, traumatic brain injury

AMS subject classifications. 65Nxx, 65Mxx, 65Zxx, 76Nxx, 35Qxx

1. Introduction.

A recent collaboration with experimentalists studying traumatic brain injury (TBI) at the Seattle Veterans Administration (VA) Hospital brought to our attention the need for very specific numerical methods [9]. Many experiments performed by the TBI community, as well as in other biomedical disciplines, employ a shock-tube, where they introduce samples to be studied after being exposed to a shock wave. These samples can vary from transwells filled with aqueous solution and cell culture to live mice [6, 9, 15, 16, 17, 20, 21, 37]. Within the shock-tube, the shock wave travels through highly compressible gas before hitting the sample, typically a nearly incompressible material with a fixed location in space. The physical effects of the shock wave hitting the sample are not usually evident from experimental data nor easy to obtain through experimental techniques.

The methods presented in this paper were motivated by this application, although they may be useful in other contexts as well. In order to successfully model the shock wave/sample interaction, we develop numerical methods that can couple the shock wave dynamics in compressible gas with almost incompressible materials, like plastic, water or even bone and brain. Some of these methods have already been employed in our recent collaboration [9]. In the present paper, we give a detailed explanation of the numerical methods and their implementation; we extend them to more complicated interface geometries, enhance their stability in highly refined grids, improve their resolution and efficiency using adaptive mesh refinement (AMR), and further study their convergence. This work will refer to [9] in the sections where it is relevant. Although our simulations can only model idealized scenarios, they can help provide detailed insight into the behavior of the shock wave interaction with

*This work was supported in part by NSF grant DMS-1216732 (RJL, MdR) and National Council of Science and Technology of Mexico [CONACyT] (MdR).

†Department of Applied Mathematics, University of Washington, Seattle, WA 98195-3925 (maojrs@uw.edu, rjl@uw.edu).

interfaces. For instance, in our previous work [8, 9], we obtain the dynamics of a shock wave impacting an interface that models a specific TBI experiment. It also strongly suggested cavitation as a possible damage mechanism, an issue that has been a subject of extense study among the TBI community [9, 15, 27, 30, 31, 32, 33, 35, 50].

Although there is an extensive body of work on computational fluid dynamics with interfaces that is relevant and might be applicable to this type of problems, such as [4, 12, 17, 28, 34, 38, 39, 46, 48] among others, the novel methods presented here are tailored to specifically model a set of experiments performed with a shock tube.

The methods presented here are based on finite volume methods for hyperbolic problems in their wave propagation form [25] and implemented into Clawpack 5.2.2 [5]. The key ingredient in these methods is the Riemann solver, which must be specifically designed to deal with highly nonlinear waves interacting with interfaces between materials having very different properties.

In Section 2, we present the Euler Equations coupled with the Tammann Equation of State (EOS), which can be used to model the various materials involved. In Section 3, we develop the one-dimensional numerical method in detail, also discussing its implementation in Clawpack [5]. The exact solution in this section is also relevant for the verification studies in Section 5. In Section 4, we extend the numerical methods to apply them to the three-dimensional (2D axisymmetric) model and on mapped grids, allowing more complicated interface geometries. Furthermore, the code was designed to employ Clawpack's adaptive mesh refinement (AMR) [2] to improve efficiency and resolution. We also discuss the inclusion of transmission-based limiters to reduce numerical oscillations in heavily refined grids produced at the interface corner. In Section 5, we summarize a verification study for the one-dimensional case [9] and perform a convergence analysis for the two-dimensional method. We also show that modifying the original minmod limiter can further reduce the numerical oscillations. The last Section discusses and summarizes some of the results and utility of these methods. Appendix A explores the question of whether a thin plastic interface between gas and liquid can be ignored altogether in numerical studies of shock tube experiments [8]. Analysis based on the nonlinear case using the numerical methods from Section 3 suggests it can be ignored. As verification, an analysis based on exact solutions to the linear acoustics equations confirms the result.

The numerical methods and implementation details are explained in this paper; the code is available in GitHub with a BSD license [7].

2. The model. We use the nonlinear compressible Euler equations for compressible inviscid flow, which allow accurate modeling of shock wave formation and propagation. These equations model the conservation of mass, momentum, and energy and provide a direct connection to temperature, which may be important for some biomedical experiments. In this type of experiment, we are not concerned with large-scale movement of the fluid, so viscosity does not play an important role; therefore, employing the inviscid equations is appropriate. In order to model different materials, we use different parameters in the equations of state (EOS) for each material, so we can model the different materials with the same equations. The equations are solved using the methods explained in Section 3.

An additional advantage of experiments performed in a shock tube is that they often exhibit cylindrical symmetry along the axis that goes through the center of the shock tube. This simplifies the three-dimensional equations into two-dimensional axisymmetric Euler equations, which in cylindrical coordinates (r,θ,z) take the form

$$\frac{\partial}{\partial t}\begin{bmatrix}\rho\\ \rho u_r\\ \rho u_z\\ E\end{bmatrix}+\frac{\partial}{\partial r}\begin{bmatrix}\rho u_r\\ \rho u_r^2+p\\ \rho u_r u_z\\ u_r(E+p)\end{bmatrix}+\frac{\partial}{\partial z}\begin{bmatrix}\rho u_z\\ \rho u_r u_z\\ \rho u_z^2+p\\ u_z(E+p)\end{bmatrix}=\begin{bmatrix}-(\rho u_r)/r\\ -(\rho u_r^2)/r\\ -(\rho u_r u_z)/r\\ -u_r(E+p)/r\end{bmatrix}, \tag{2.1}$$

where ρ is the density; u_r and u_z denote the velocities in the radial and axial direction, r and z respectively; E is the total energy and p is the pressure. These equations have the same form as the two-dimensional Euler equations with the addition of geometrical source terms (the right hand side), and are discussed further in Section 4.

2.1. Tammann equations of state. The system of equations (2.1) is closed with the addition of an EOS. It is usually given as a relation between pressure, density and specific internal energy, i.e. $p = p(\rho, e)$. The most well known EOS is the one for an ideal gas $p = (\gamma - 1)\rho e$, where γ is the ratio of heat capacities. While this EOS is very good for describing the behavior of most gases, it is not appropriate for modeling nearly incompressible materials like water or some elastic solids.

Several alternatives exist; in this work, we will use the stiffened gas EOS, also known as the Tammann EOS. This equation of state is very useful to model a wide range of fluids even in the presence of strong shock waves [11]. The Tammann EOS is given by

$$p = (\gamma - 1)\rho e - \gamma p_\infty, \tag{2.2}$$

where γ and p_∞ can be determined experimentally for different materials. The internal energy e is related to the total energy E by $E = \rho e + \frac{1}{2}\rho u \cdot u$. The Tammann EOS and the ideal gas EOS are the same except for the extra term $-\gamma p_\infty$, where $\gamma,\ p_\infty > 0$. For fluids with $p_\infty \gg p_{atm}$ (atmospheric pressure), the relative change in density, when changing the pressure, is very small. Consequently, the Tammann EOS is a good approximation for nearly incompressible fluids and can also be used to model acoustic waves in some elastic solids, like plastic. For sufficiently weak shocks the Tammann EOS can be further simplified to the Tait EOS, see [11], but for greater generality we use the Tammann EOS. Table 2.1 shows the Tammann EOS parameters for the materials used in the simulations here presented.

Material	γ	$p_\infty(GPa)$
Air (Ideal gas EOS)	1.4	0.0
Plastic (polystyrene)	1.1	4.79
Water	7.15	0.3

Table 2.1: Parameters for the Tammann EOS to model the different materials. Note the p_∞ values for plastic and water are in GPa and are several orders of magnitude above the atmospheric pressure. The parameters for air and water were taken from [11]. As polystyrene is a solid, γ was chosen to be close to 1, and p_∞ was adjusted to yield the right speed of sound in polystyrene [29].

3. Numerical methods. The Euler equations are a nonlinear hyperbolic system of conservation laws, so they can be efficiently solved with high-resolution shock-capturing finite volume methods (FVM). This is done by using the wave propagation

algorithms described in [25] and implemented in Clawpack [5]. The fundamental problem to solve at each cell interface of our computation is the well known Riemann problem. A general one-dimensional Riemann problem for a system of conservation laws like Euler equations can be stated as

$$q + f(q)_x = 0, \tag{3.1}$$
$$q(x,0) = \begin{cases} q_l & \text{if } x < 0 \\ q_r & \text{if } x > 0, \end{cases}$$

The Euler equatons in this work are solved by implementing a hybrid Riemann HLLC-exact type approximate solver for one-dimensional Euler equations with interfaces. This solver couples an HLLC approximate Riemann solver to an exact Riemann solver for the Tammann EOS and an Eulerian-Lagrangian description coupling at the interface. As the interfaces are represented by contact discontinuities, the HLLC solver is ideal to deal accurately with interface problems. Furthermore, the exact solver will serve as a reference solution to verify the numerical method.

From the well-known solution to the Euler equations for an ideal EOS [25, 45], we expect our solution will consist of two acoustic waves, the 1-wave and 3-wave (rarefactions or shocks), and a contact discontinuity, the 2-wave between them. The n-wave refers to the wave corresponding to the n-characteristic field (see [25]). This will separate our system in four states, q_l, q_{*l}, q_{*r}, q_r. The left state q_l will be connected to the state q_{*l} by a 1-wave, a shock wave or a rarefaction. The state q_{*l} and q_{*r} will be connected by a 2-wave, the contact discontinuity with equal pressure p_* and velocity u_* but different density on both sides. The states q_{*r} and q_r are connected by a 3-wave, which is a shock wave or a rarefaction.

The method can be extended to two dimensions by using dimensional splitting or transverse solvers. The geometrical source terms can be resolved using a splitting method [25, 26]. In the next paragraphs, we give an overview of the modified HLLC Riemann solver and the exact Riemann solver for the Tammann EOS with discontinuous parameters.

3.1. A modified HLLC solver. The HLLC (Harten-Lax-van Leer-Contact) solver is an approximate Riemann solver for Eq. (3.1). The main idea of the HLLC solver is, given the left and right going wave speeds S_l and S_r by some algorithm or approximation, assume a wave configuration of three waves separating four constant states. The Riemann solution to the one-dimensional Euler equations consists of three waves, two acoustic waves with a contact discontinuity in between. The approximate solution for this method will be of the form

$$\tilde{q}(x,t) = \begin{cases} q_l & \text{if } \frac{x}{t} \le S_l \\ q_{*l} & \text{if } S_l \le \frac{x}{t} \le S_*, \\ q_{*r} & \text{if } S_* \le \frac{x}{t} \le S_r, \\ q_r & \text{if } \frac{x}{t} \ge S_r, \end{cases}$$

where S_* is the approximate wave speed of the contact discontinuity. Assuming we can obtain S_l and S_r, we only need to find q_{*l}, q_{*r} and S_* to solve the problem. These quantities can be obtained by integrating over a box in the x, t plane using the Rankine-Hugoniot conditions and assuming constant pressure and normal velocity across the contact discontinuity, see [45]. The desired states and contact discontinuity

speed are given by

$$q_{*k} = \frac{S_k q_k - f_k + p_* D}{S_l - S_*}, \quad \text{with:} \quad D = [0, 1, S_*],$$
$$S_* = \frac{p_r - p_l + \rho_l u_l (S_l - u_l) - \rho_r u_r (S_r - u_r)}{\rho_l (S_l - u_l) - \rho_r (S_r - u_r)},$$

where ρ_k, u_k with $k = l, r$ are the left or right density and speed in the Euler equations [45].

In order to calculate the wave speeds S_l and S_r, we will need to calculate the sound speed. This is where we require the EOS. A simple estimate is the one given by Davis [45] as

$$S_l = \min\{u_l - c_l, u_r - c_r\} \quad S_r = \max\{u_l + c_l, u_r + c_r\},$$

where u_k is the normal velocity and c_k is the sound speed on each side, $k = l, r$. Note that the easiest way to calculate the speed of sound is using the EOS $p = p(\rho, e)$. It is usually given in the form,

$$c = \sqrt{\frac{\partial p(\rho, e)}{\partial \rho}\bigg|_s} = \sqrt{\frac{\partial p(\rho, e)}{\partial \rho} + \frac{p(\rho, e)}{\rho^2} \frac{\partial p(\rho, e)}{\partial e}}, \tag{3.2}$$

where s is the entropy, and the first derivative is taken along the isentropic curve. A possible improvement is to employ Roe averages in wave speed estimates $S_l = \min\{u_l - c_l, \tilde{u} - \tilde{c}\} \quad S_r = \max\{\tilde{u} + \tilde{c}, u_r + c_r\}$ where $\tilde{u}$ and $\tilde{c}$ are the Roe averages of the normal velocity and speed of sound respectively [10]. These Roe averages can be calculated using different configurations. Some might be more accurate when dealing with interfaces, as pointed out in [19].

The HLLC solver just discussed works well for the one-dimensional Euler equations with an ideal gas EOS. However, we want to implement the HLLC solver with the Tammann EOS across an air-water or air-plastic interface. The difference between the parameters for different materials in the Tammann EOS are of several orders of magnitude as shown in Table 2.1. This generates instabilities in the HLLC solver, more so in the multi-dimensional setting. The instability is generated because we model the interfaces as being fixed in space; however, there is always a displacement of the contact discontinuity, i.e. the interface, even when the material is almost incompressible. The displacement is very small indeed, but it is big enough to render our numerical method unusable. In order to solve this issue, we model each material in Eulerian coordinates using the usual HLLC solver; if any of the cells is next to the interface, we modify our original HLLC or exact solver to work in Lagrangian coordinates, where the interface is actually fixed with respect to the reference frame. This is done by displacing the frame of reference by S_*,

$$\tilde{S}_l = S_l - S_* \quad \tilde{S}_* = 0 \quad \tilde{S}_r = S_r - S_* \tag{3.3}$$

For instance, assume we are running a one-dimensional simulation of the Euler equations, with a fixed interface modeled by a jump in the parameters of the EOS. The interface is aligned to the edge between cells i and $i + 1$, the transformed Riemann solver will be as shown in Figure 3.1. This will ensure the contact discontinuity velocity is zero and consequently, the interface is modeled as fixed. The wave contributions will be the correct ones since we are just modifying the wave velocity and not the solution q's. There is, of course, an error made at the interface when coupling the two

descriptions; however, as the displacements of the interface are very small due to very low compressibility, this error is small, and it doesn't cause instabilities as before.

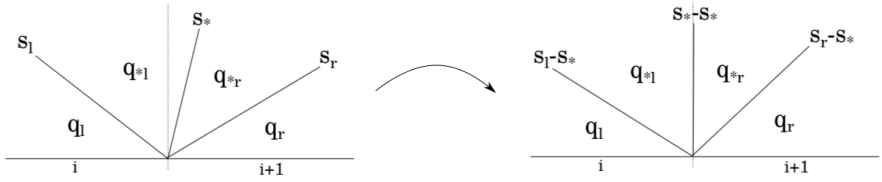

Fig. 3.1: Transformation for the HLLC Riemann solver between grid cells i and $i+1$ from Eulerian coordinates to Lagrangian coordinates. The transformation can be employed for other Riemann solvers too.

In order to provide better accuracy along the interface, we will also implement an exact Riemann solver for the Tammann EOS. The HLLC solver will be used to model each of the materials in Eulerian coordinates, and the exact solver will be used to solve the Riemann problems at the interface. The transformation to Lagrangian coordinates for the exact solver is equivalent to the one in (3.3).

3.2. Exact Riemann solver for Tammann EOS with a jump in the parameters. The Riemann problem (3.1) sometimes can also be solved exactly; the form of the solution will depend on the equations and the EOS being used. An exact solver for the Euler equations coupled with the Tammann EOS for constant parameters was given by Ivings & Toro [22]. In the next paragraphs, we obtain the exact Riemann solver for the Euler equations coupled with the Tammann EOS with different constant parameters on the left and right states. This can be extended numerically to general varying parameters, by averaging them on each cell and using this Riemann solver to provide the solution. The solver is based on the one provided in [22]; however, it extends it to include a jump in the Tammann EOS parameters between the left and right state.

We consider the one-dimensional Riemann problem for the Euler equations with the Tammann EOS. We want to solve the one-dimensional Euler equations,

$$\begin{bmatrix} \rho \\ \rho u \\ E \end{bmatrix}_t + \begin{bmatrix} \rho u \\ \rho u^2 + p \\ u(E+p) \end{bmatrix}_x = 0, \tag{3.4}$$

where ρ is density, u velocity, E the internal energy and p the pressure and the subcripts x, t denote partial derivatives with respect x and t. The Tammann EOS is given by $p = \rho e(\gamma_k - 1) - \gamma_k p_{\infty k}$ where e the specific internal energy and $k = l, r$ determines which coefficients to use for the EOS. The initial conditions are given by the left and right constant states $q_l = [\rho_l, \rho_l u_l, E_l]$ and $q_r = [\rho_r, \rho_r u_r, E_r]$. Note that the state of the system can also be written in terms of the primitive variables $[\rho, u, p]$ by using the equation of state.

As we mentioned before, the solution of the Euler equations will consist of the 1-wave and 3-wave (rarefactions or shocks), and a contact discontinuity, the 2-wave between them. The system will have four different solution states, q_l, q_{*l}, q_{*r}, q_r separated by the three waves. In order to figure out if the 1-wave and 3-wave are rarefactions or shocks, we will need to create a function of the middle state pressure p_* that

ensures the velocity u_* across the contact discontinuity is consistent. As we know the velocity on the left state u_l should be connected by a rarefaction or shock to u_*, we can calculate $u_* = u_l + [u]_1$ with $[u]_1$the jump of the velocity across the 1-wave. In a similar manner, we also know the 3-wave should be a shock or rarefaction, so we can calculate $u_* = u_r - [u]_3$; therefore, we define

$$\begin{aligned} \phi_l(p_*) &= u_* = u_l - \mathcal{F}_l(p_*), \\ \phi_r(p_*) &= u_* = u_r + \mathcal{F}_r(p_*). \end{aligned} \tag{3.5}$$

where $\mathcal{F}_{l,r}(p_*) = -[u]_{1,3}$ will change form depending if it's a shock or a rarefaction (signs were chosen for notation consistency). As we expect these two equations yield the same contact discontinuity velocity u_*, then

$$\Phi(p_*) = \phi_r(p_*) - \phi_l(p_*) = 0. \tag{3.6}$$

This nonlinear equation for p_* will yield the pressure p_* that provides consistency between the type of waves (rarefactions or shocks), their speeds and the contact discontinuity velocity u_*. As we mentioned before, the shape of $\phi_k(p_*)$ will depend on whether the states are connected by a shock wave or rarefaction. Once the p_* has been found, the contact discontinuity velocity can be found from (3.5). The only remaining quantity to calculate from the primitive variables is the density. Furthermore, we also need the speeds of the 1-wave and 3-wave. Once we write the explicit equations for our system, it will be clear how to obtain these quantities.

Before writing the equations explicitly, we should first note that having a rarefaction or shock in the 1-wave and 3-wave will depend on the pressure p_*. How can we know which one, can be answered by simple physical intuition. If the pressure is higher on the side toward which the wave is propagating, it will yield a rarefaction. If the pressure is lower, it will be a shock. In the Euler equations, this yields four possible cases for the value $\Phi(p_*)$ of equation (3.6), just as in the solution using the ideal gas EOS [22, 25]:

- 1-rarefaction, 3-rarefaction: $p_* < p_l$ and $p_* < p_r$
  $\Phi(p_*) = \phi_r^R(p_*) - \phi_l^R(p_*)$,
- 1-shock, 3-rarefaction $p_l \leq p_* \leq p_r$
  $\Phi(p_*) = \phi_r^R(p_*) - \phi_l^S(p_*)$,
- 1-rarefaction, 3-shock $p_r \leq p_* \leq p_l$
  $\Phi(p_*) = \phi_r^S(p_*) - \phi_l^R(p_*)$,
- 1-shock, 3-shock: $p_* > p_l$ and $p_* > p_r$
  $\Phi(p_*) = \phi_r^S(p_*) - \phi_l^S(p_*)$,

where the index S, R indicates if the ϕ was obtained by using the Rankine-Hugoniot equations to connect states by shocks or the Riemann invariants to connect them by rarefactions respectively.

In the next paragraphs, we derive the functions ϕ_k^μ for all the four cases with $k = l, r$ and $\mu = R, S$. We show how to obtain the density and the missing wave speeds. In order to do so, we employ the Rankine-Hugoniot equations and the Riemann invariants. We will denote the speed of the 1-wave, S_l, the 2-wave, S_*, and the 3-wave S_r.

3.2.1. Rankine-Hugoniot conditions for shock waves. As we know the 1-wave and the 3-wave could each be a shock. In that case, the velocity of the wave, i.e. the shock, will be given by the Rankine-Hugoniot conditions. We will generalize

this method for the 1-wave velocity S_l and the 3-wave velocity S_r, by employing S_k, with $k = l, r$.

The Rankine-Hugoniot conditions are in general given by $S_k\,(q_k - q_{*k}) = f(q_k) - f(q_{*k})$, where q is the vector state variable, $f(q)$ the vector state flux and S_k the shock velocity. For the Euler equations this can be easily rewritten as [22],

$$\rho_k \omega_k = \rho_{*k} \omega_*, \tag{3.7}$$

$$\rho_k \omega_k^2 + p_k = \rho_{*k} \omega_*^2 + p_{*k}, \tag{3.8}$$

$$\frac{1}{2}\omega_k^2 + h_k = \frac{1}{2}\omega_*^2 + h_{*k}, \tag{3.9}$$

where $k = l, r$, $\omega_k = u_k - S_k$, $\omega_* = u_* - S_k$ and the specific enthalpy is given by $h = e + (p + p_\infty)/\rho$ with e the specific internal energy that relates to the internal energy of our original variables by $E = \rho e + \rho u^2/2$. We will use these relations to find the $\phi_K^S(p_*)$ of equation (3.6) and the wave speeds S_k.

Finding $\phi_l^S(p_*)$ and $\phi_r^S(p_*)$ and S_l and S_r: We can start by defining the mass fluxes $\mathcal{Q}_k$ for $k = l, r$ as

$$\mathcal{Q}_l = \rho_l \omega_l = \rho_{*l} \omega_* \tag{3.10}$$

$$\mathcal{Q}_r = -\rho_r \omega_r = -\rho_{*r} \omega_*. \tag{3.11}$$

As $\omega_k = u_k - S_k$, from these two equations we can obtain the wave speeds in terms of Q_l and $\mathcal{Q}_r$,

$$S_l = u_l - \frac{\mathcal{Q}_l}{\rho_l}, \quad S_r = u_r + \frac{\mathcal{Q}_r}{\rho_r}. \tag{3.12}$$

Though, we still need to find $\mathcal{Q}_l$ and $\mathcal{Q}_r$, so we substitute equation (3.10) and (3.11) into (3.8) to immediately obtain

$$\mathcal{Q}_l = \frac{\tilde{p}_{*l} - \tilde{p}_l}{\omega_l - \omega_*} = \frac{p_* - p_l}{u_l - u_*} \tag{3.13}$$

$$\mathcal{Q}_r = -\frac{\tilde{p}_{*r} - \tilde{p}_r}{\omega_r - \omega_*} = -\frac{p_* - p_r}{u_r - u_*}, \tag{3.14}$$

where $\tilde{p}_\kappa = p_\kappa + p_{\infty\kappa}$ is defined to simplify future notation with $\kappa = l, *l, *r$ and r. Note that $\tilde{p}_{*l} \neq \tilde{p}_{*r}$ and that $\tilde{p}_{*k} - \tilde{p}_k = p_* - p_k$ since $p_* = p_{*l} = p_{*r}$ and $p_{\infty k} = p_{\infty *k}$ $(k = l, r)$. Solving for u_* we obtain the equations,

$$\begin{aligned} u_* &= u_l - \frac{\tilde{p}_{*l} - \tilde{p}_l}{\mathcal{Q}_l} = \phi_l^S(p_*) \\ u_* &= u_r + \frac{\tilde{p}_{*r} - \tilde{p}_r}{\mathcal{Q}_r} = \phi_r^S(p_*) \end{aligned} \tag{3.15}$$

Comparing to equations (3.5), we notice $\mathcal{F}_k(p_*) = \frac{p_* - p_k}{\mathcal{Q}_k}$. We also notice we have almost obtained the ϕ functions we are looking for, though we still need to find $\mathcal{Q}_l$ and $\mathcal{Q}_r$ in terms of known variables.

Finding $\mathcal{Q}_l$ and $\mathcal{Q}_r$: From equations (3.10) and (3.13), we know that

$$\frac{\tilde{p}_{*l} - \tilde{p}_l}{\omega_l - \omega_*} = \rho_l \omega_l.$$

Solving for ω_*, substituting the solution into (3.10) and subtituting the w_l for $\mathcal{Q}_l/\rho_l$, we obtain a new equation that we can solve for $\mathcal{Q}_l$ that yields,

$$\mathcal{Q}_k = \sqrt{\rho_k \rho_{*k} \frac{\tilde{p}_{*k} - \tilde{p}_k}{\rho_{*k} - \rho_k}}. \tag{3.16}$$

with $k = l, r$, since we repeated the same process for $\mathcal{Q}_r$ and obtained exactly the same equation. However, we still don't know ρ_{*k}, for this we will need our third Rankine-Hugoniot condition (3.9).

Finding ρ_{*l} and ρ_{*r}: From equation (3.9), we can obtain

$$\begin{aligned} h_{*k} - h_k &= \frac{1}{2}\left(w_k^2 - w_*^2\right) \\ &= \frac{1}{2}\left(\pm\frac{\mathcal{Q}_k^2}{\rho_k^2} \mp \frac{\mathcal{Q}_k^2}{\rho_{*k}^2}\right) \\ &= \frac{1}{2}\left(\frac{1}{\rho_k} + \frac{1}{\rho_{*k}}\right)(\tilde{p}_{*k} - \tilde{p}_k), \end{aligned} \tag{3.17}$$

where the sign above is used for $k = l$ and the one below for $k = r$, and we used equations (3.10) and (3.11) for the second line and (3.16) for the third line. We can now substitute the specific enthalpy $h = \gamma\tilde{p}/(\rho(\gamma - 1))$ in equation (3.17) to obtain,

$$\frac{\gamma_{*k}}{\gamma_{*k} - 1}\frac{\tilde{p}_{*k}}{\rho_{*k}} - \frac{\gamma_k}{\gamma_k - 1}\frac{\tilde{p}_k}{\rho_k} = \frac{1}{2}\left(\frac{1}{\rho_k} + \frac{1}{\rho_{*k}}\right)(\tilde{p}_{*k} - \tilde{p}_k).$$

As the interface is the contact discontinuity, the jump in the parameters is only across the contact discontinuity, so $\gamma_{*k} = \gamma_k$. Now we can solve for the unknown density,

$$\rho_{*k} = \rho_k \left(\frac{\frac{\tilde{p}_*}{\tilde{p}_k} + \frac{\gamma_k - 1}{\gamma_k + 1}}{\frac{\tilde{p}_*}{\tilde{p}_k}\frac{\gamma_k - 1}{\gamma_k + 1} + 1}\right). \tag{3.18}$$

Replacing this result into equation (3.16), we obtain $\mathcal{Q}_k$ in terms of p_* and known variables,

$$\mathcal{Q}_k = \sqrt{\rho_k \frac{\tilde{p}_{*k} + \tilde{p}_k \frac{\gamma_k - 1}{\gamma_k + 1}}{\frac{2}{\gamma_k + 1}}}. \tag{3.19}$$

With equations (3.15) and (3.19), we can calculate the $\phi_{l,r}^S$ nonlinear functions of p_* in terms of known variables. The functions $\phi_{l,r}^S$ allow us to construct equation (3.6) and solve it using a Newton method or other root finder in order to obtain the value of p_*. Equations (3.15) will then yield the contact discontinuity speed $S_* = u_*$ in terms of p_*. Further on, we can calculate $\mathcal{Q}_l$ and $\mathcal{Q}_r$ from (3.19), and we can substitute in (3.12) to obtain the corresponding wave speeds. However, this will only solve the 4th case of equation (3.6), 1-shock and 3-shock solution. If any of our waves happens to be a rarefaction, we will also need to calculate the $\phi_{l,r}^R$ functions. This will be obtained using the Riemann invariants.

3.2.2. Riemann invariants for rarefaction waves. Riemann invariants are variables that remain constant through simple waves such as rarefactions. The Riemann invariants across the 2-wave are the pressure p_* and the normal velocity u_*. The Riemann invariants for the 1-wave and 3-wave are the entropy and the quantities,

$$u_l + \frac{2c_l}{\gamma_l - 1} = u_* + \frac{2c_{*l}}{\gamma_l - 1}, \tag{3.20}$$

$$u_r - \frac{2c_r}{\gamma_r - 1} = u_* - \frac{2c_{*r}}{\gamma_r - 1}, \tag{3.21}$$

correspondingly. The speed of sound c_K is obtained by applying equation (3.2) to the Tammann EOS,

$$c_k = \sqrt{\gamma_k \frac{p_k + p_{\infty k}}{\rho_k}}. \tag{3.22}$$

As the entropy is invariant, we can use the Tammann EOS isentropic relation to obtain the density in the middle states,

$$\rho_{*k} = \rho_k \left(\frac{\tilde{p}_{*k}}{\tilde{p}_k} \right)^{1/\gamma}. \tag{3.23}$$

Solving (3.20) and (3.21) for u_* and using equations (3.22) and (3.23), we immediately obtain

$$u_* = u_l + \frac{2c_l}{\gamma_l - 1} \left[1 - \left(\frac{\tilde{p}_{*l}}{\tilde{p}_l} \right)^{\frac{\gamma_l - 1}{2\gamma_l}} \right] = \phi_l^R(p_*),$$

$$u_* = u_r - \frac{2c_r}{\gamma_r - 1} \left[1 - \left(\frac{\tilde{p}_{*r}}{\tilde{p}_r} \right)^{\frac{\gamma_r - 1}{2\gamma_r}} \right] = \phi_r^R(p_*).$$

As $\tilde{p}_\kappa = p_\kappa + p_{\infty\kappa}$, when we compare to equations (3.5) we obtain the $\phi_{l,r}^R$ functions. The rarefaction head velocities will be given by $u_l - c_l$ and $u_r + c_r$; the tail velocities will be $u_* - c_{*l}$ and $u_* + c_{*r}$. For numerical purposes, a simple approximate velocity is provided for S_l and S_r as the average between the head and tail velocity.

In order to compute the complete structure of the rarefaction wave [22, 25], we can use the Riemann invariants from Eqs. 3.20 and 3.21, along with Eq. 3.22 and the isentropic relation from Eq. 3.23. The solution for the 1-rarefaction wave along the rays $x/t = \xi = u_{rar1} - c_{rar1}$ is then

$$u_{rar1}(\xi) = \frac{u_l(\gamma_l - 1) + 2(\xi + c_l)}{\gamma_l + 1},$$

$$\rho_{rar1} = \rho_l \left[\frac{u_{rar1}(\xi) - \xi}{c_l} \right]^{\frac{2}{\gamma_l - 1}},$$

$$p_{rar1} = \tilde{p}_l \left[\frac{u_{rar1}(\xi) - \xi}{c_l} \right]^{\frac{2\gamma_l}{\gamma_l - 1}} - p_{\infty l},$$

and for a 3-rarefaction wave along the rays $x/t = \xi = u_{rar3} + c_{rar3}$ is,

$$u_{rar3}(\xi) = \frac{u_r(\gamma_r - 1) + 2(\xi - c_r)}{\gamma_r + 1},$$
$$\rho_{rar3} = \rho_r \left[\frac{u_{rar3}(\xi) - \xi}{c_r}\right]^{\frac{2}{\gamma_r - 1}},$$
$$p_{rar3} = \tilde{p}_r \left[\frac{u_{rar3}(\xi) - \xi}{c_r}\right]^{\frac{2\gamma_r}{\gamma_r - 1}} - p_{\infty r}.$$

Now that we know the functions $\phi_{l,r}^{s,r}$ for the rarefactions, we can construct the function $\Phi(p_*)$ function from (3.6) for any of the 4 possible scenarios. The value of p_* will be found by numerically finding the roots of $\Phi(p_*) = 0$. Note which case to employ to calculate $\Phi(p_*)$ might change in each iteration of the root finder. Once p_* is found, u_*, ρ_{*l}, ρ_{*r}, S_l and S_r can be found using the relations we just derived depending if it's a shock or a rarefaction. As we know the three wave speeds S_l, S_* and S_r and the primitive variables $[\rho, u, p]$ on all the 4 states for all the possible cases, we have the solved the Riemann problem.

3.3. Implementation into Clawpack. These methods are implemented into the Clawpack 5.2.2 software [5]. This software employs Godunov's method [14] with high order corrections and limiters to better handle discontinuities[25]. In order to implement these methods into Clawpack, we need to write Godunov's method in the wave propagation form. Consider a state vector $q(x,t)$, a one dimensional conservation law is given by $q_t + f(q)_x = 0$. We partition the space in cells with index i and consider the cell average at time t to be $Q_i^n = \int_{x_{i-1/2}}^{x_{i+1/2}} q(x, t_n)dx$. Then the Godunov method is given by,

$$Q_i^{n+1} = Q_i^n - \frac{\Delta t}{\Delta x}(\underbrace{\mathcal{A}^- \Delta Q_{i+1/2}}_{\text{LeftEdge}} + \underbrace{\mathcal{A}^+ \Delta Q_{i-1/2}}_{\text{RightEdge}}) - \underbrace{\frac{\Delta t}{\Delta x}\left(\tilde{F}_{i+1/2} - \tilde{F}_{i-1/2}\right)}_{\text{HighResolution}}, \tag{3.24}$$

with,

$$\tilde{F}_{i\pm 1/2} = \frac{1}{2}\sum_{p=1}^{m} |s_{i\pm 1/2}^p| \left(1 - \frac{\Delta t}{\Delta x}|s_{i\pm 1/2}^p|\right) \underbrace{\widetilde{\mathcal{W}}_{i\pm 1/2}^p}_{\text{Limiter}}, \tag{3.25}$$

where $\mathcal{A}^- \Delta Q_{i\pm 1/2} = \sum_{p=1}^m (s_{i\pm 1/2}^p)^- \mathcal{W}_{i\pm 1/2}^p$ and $\mathcal{A}^+ \Delta Q_{i\pm 1/2} = \sum_{p=1}^m (s_{i\pm 1/2}^p)^+ \mathcal{W}_{i\pm 1/2}^p$ are the left and right going fluctuations of the edge of cell $i \pm 1/2$ respectively, with $(s_{i\pm 1/2}^p)^\pm$ indicating only those values of $s_{i\pm 1/2}^p$ with sign $\pm$, m is the number of waves, $s_i^p \mp 1/2$ is the velocity of the p characteristic of the Riemann problem at edge $i \mp 1/2$, the wave $\mathcal{W}_{i\mp 1/2}^p$ corresponds to the jump across that characteristic and $\widetilde{\mathcal{W}}_{i\pm 1/2}^p$ is the limited version of the wave, see [25] for more details.

The numerical solution requires solving a Riemann problem on each cell edge of our partition in order to obtain the fluctuations. The Riemann solutions presented previously have provided the characteristic velocities s^p, and we can calculate the waves $\mathcal{W}^p$ by calculating the jump of q across the p characteristic. This information is calculated for each cell edge and fed into Clawpack, where the method from Eq. 3.24 is implemented. Appendix A contains one-dimensional implementations of these methods. In the next Sections, we will study two-dimensional implementations.

4. Two dimensional axisymmetric model. The three dimensional Euler Equations with cylindrical symmetry can be solved as two dimensional axisymmetric Euler Equations with additional source terms, see Eqs. 2.1 and Figure 4.1. The conservation law for $q(x, y, t)$ takes the form $q_t + f(q)_x + g(q)_y = \psi(q, x, y, t)$. In two dimensions, the numerical cell average is calculated as $Q^n_{i,j} = \frac{1}{\Delta y \Delta x} \int_{C_{i,j}} q(x, y, t_n) dx dy$, where $C_{i,j}$ is the cell $[x_{i-1/2}, x_{i+1/2}] \times [y_{j-1/2}, y_{j+1/2}]$. The source terms can be solved using a fractional-step method [25] by alternating between $q_t + f(q)_x + g(q)_y = 0$ and $q_t = \psi(q, x, y, t)$. The latter is an ordinary differential equation, which has an exact solution in the case of Equations 2.1, as shown in [9]. More complex source terms might require implementing another time stepping method like Runge-Kutta or TR-BDF2. In a similar manner, the simplest approach to solve the two dimensional system $q_t + f(q)_x + g(q)_y = 0$ is dimensional splitting. This is done again with a fractional-step method to split the two dimensional problem up into a sequence of one-dimensional problems alternating between solving $q_t + f(q)_x = 0$ and $q_t + g(q)_y = 0$. For more details and different splitting algorithms see [25].

Although dimensional splitting is simple to implement, we can obtain second-order accuracy and less numerical smearing simultaneously by using transverse propagation algorithms from [24]. This will require splitting the normal wave fluctuations $\mathcal{A}^{\pm}\Delta Q_{i\pm1/2,j}$ at edge $i \pm 1/2$ into transverse wave fluctuations $\mathcal{B}^{\pm}\mathcal{A}^{+}\Delta Q_{i\pm1/2,j}$ and $\mathcal{B}^{\pm}\mathcal{A}^{-}\Delta Q_{i\pm1/2,j}$. If the normal direction is x, then the normal fluctuations are calculated with the flux $f(q)$ and the transverse ones with the flux $g(q)$. Our specific model will require a very special kind of transverse solvers, which have been implemented in [9]; a generalized version of these solvers will be explored in detail later in this paper.

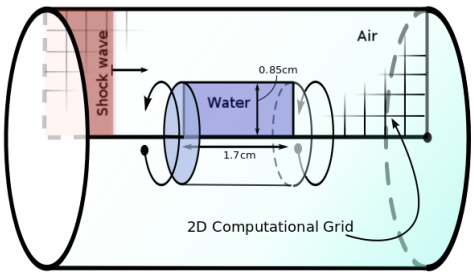

Fig. 4.1: The axisymmetric model is obtained by revolving the 2D computational grid. The inner square corresponds to the air-water interface. The inside part is filled with water and the outside part is filled with air. All the outer boundaries are modeled with non-reflecting boundary conditions. The interface location was chosen following the source of this figure [9].

The two-dimensional axisymmetric model of Eqs. 2.1 employing a Tammann equation of state with interfaces and transverse solvers were implemented in a traumatic brain injury application in [9]. This work showed how the geometry of the interface can be very relevant and even produce cavitation effects. The set up in [9] and in this work is essentially the one shown in Figure 4.1. A cylindrical plastic container filled with water is placed inside a shock tube. The cylindrical outer boundary corresponds to a cylindrical cross section of the shock tube. The results shown in the Appendix A and in [8] show the plastic interface can be neglected in the two-dimensional model.

In this work, the model implemented in [9] is extended to work with AMR capabilities in Clawpack [5, 2]. The AMR implementation requires interpolating the value from coarser grid cells into the finer ones. However, when this interpolation is done across the interface, it will cause instabilities due to the big jump in the EOS parameters across the interface. In order to address this issue, we had to make sure that when a refinement patch intersects the interface, the interpolation for the finest grids is performed only using grid cells corresponding to the same material. For instance, if we need to refine a water grid cell, which is adjacent to the air interface, we will only use the values of adjacent cells corresponding to other water grid cells to obtain the interpolated values in the refined cells. It should be noted that the interface is always aligned to the cell edges, so there are no grid cells that contain two materials. This is also true for the mapped grid case studied below. Figure 4.2 shows the pressure contours for six different time points for a shock wave traveling in air and hitting a water interface fixed in space, as illustrated in Figure 4.1. The grid is plotted on top showing AMR in action with 4 levels of refinement. The first, second and third coarser grid levels are shown explicitly. The level four refinement is plotted as patches that indicate the highest refinement. Additionally, the code allows us to add gauges to observe the pressure as a function of time at any given point.

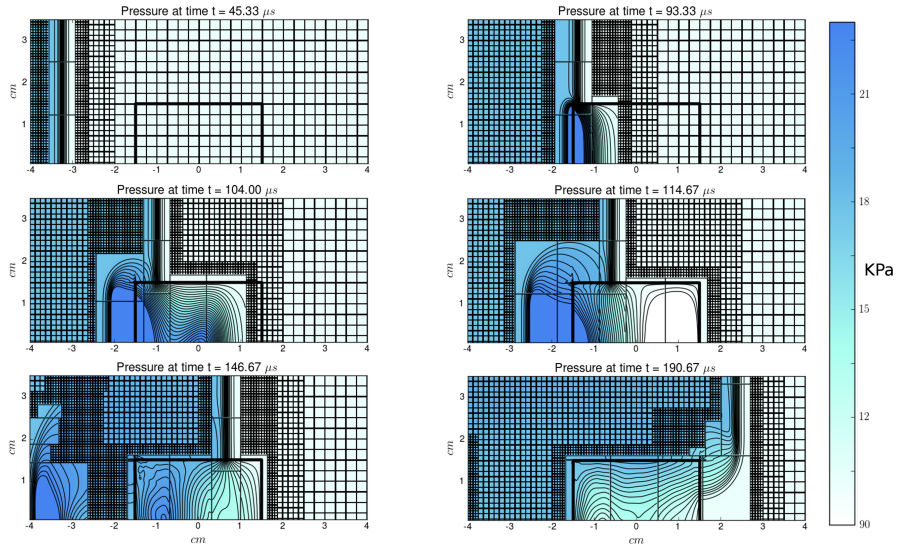
Pressure at time t = 45.33 μs
Pressure at time t = 93.33 μs
Pressure at time t = 104.00 μs
Pressure at time t = 114.67 μs
Pressure at time t = 146.67 μs
Pressure at time t = 190.67 μs
cm
KPa
21
18
15
12
90

Fig. 4.2: Axisymmetric simulation pressure contour plots at six different times points $t = 45.33, 93.33, 104, 114.67, 146.67, 190.67 \mu s$, using four levels of AMR. The parameters employed to model water and air for the Tammann EOS are the ones in Table 2.1. The pressure amplitude is given along the color bar in KPa. The interface separating air and water is marked as a thick black line, and considering the axis of symmetry is the x axis, it models a cylindrical water interface immersed in air. The shock wave travels from the left to right. The first, second and third AMR grid refinement levels are plotted explicitly while the fourth level just shows the refinement patches for clarity. The pressure contours are only shown in the highest refinement level.

In addition to the implementation of these methods in [8, 9], we now show an extension of the algorithms for a mapped grid with adaptive mesh refinement (AMR).

4.1. Two dimensional model in a mapped grid. These algorithms can also be used on a mapped grid where the quadrilateral grid cells are not necessarily rectangular. We will first consider how to implement the normal Riemann solver in the mapped grid. This will require a mapping from a Cartesian grid to a quadrilateral grid, which will tell us the normal at each cell edge where we are solving the Riemann solver as well as the scaling of the edges and the scaling of the areas of the cells. The mapped normal Riemann solver can be done using the same solver as in the Cartesian case by following these steps:

- Define a mapping;
- Use the normal at each mapped cell edge to rotate the velocities from the computational domain into normal and transverse components in the physical domain;
- Solve the Riemann problem as usual with the rotated velocities and calculate the waves;
- Rotate the waves back into the computational domain;
- Use the cell edge and area scaling to modify the algorithm in Eq. 3.24, see [25].

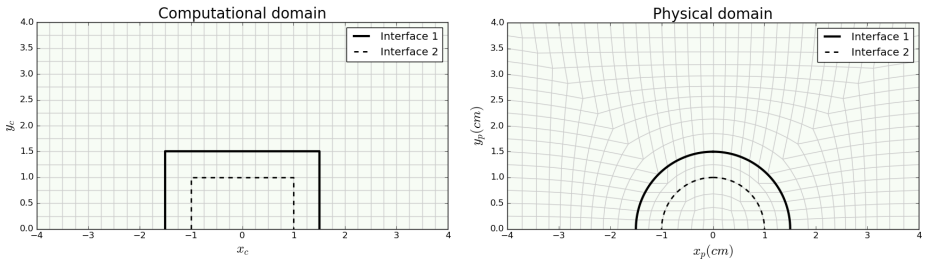

Fig. 4.3: Computational and physical mapped grid of a circular shell inclusion based on the mapping in [3]. The mapping provides two possible circular interfaces, so considering the model is axisymmetric along the x axis, it can be used to model a spherical interface or a spherical thick shell interface. The locations of two possible interfaces are shown as thick continuous and dashed lines in both domains.

The mapping of Figure 4.3 is based on the mappings of [3]. Consider a computational point (x_c, y_c) on a rectangular grid such that $x_c > 0$ and $|y_c| < x_c \equiv d$. The vertical line segment from $(d, -d)$ to (d, d) will be mapped to a circular arc with radius $R(d)$ that intersect the identity diagonals at $(D(d), -D(d))$ and $(D(d), D(d))$. The center of such a circular arc is then given by $(x_0, y_0) = (D(d) - \sqrt{R(d)^2 - D(d)^2}, 0)$, and the point in the computational grid is mapped to the physical grid point (x_p, y_p) by

$$y_p = y_c D(d)/d,$$
$$x_p = x_0 + \sqrt{R(d)^2 - y_p^2}.$$

In the mapping of Figure 4.3 we have indicated two interfaces: the inner one at radius r_i (1cm) and the outer one at radius r_o (1.5cm) from the origin. The size of the square domain in the computational grid where the mapping is applied is given by a third parameter r_m (4cm), with $r_m > r_o > r_i$. The square domain is centered at the origin and the length of each side is $2r_m$. In order to determine the mapping, we need to

choose $R(d)$ and $D(d)$ in the three regions defined by the two interfaces. One option that works well, as shown in Figure 4.3, is given by

$$D(d) = \begin{cases} r_m \frac{d}{\sqrt{2}} \\ r_m \frac{d}{\sqrt{2}} \\ \frac{r_o}{\sqrt{2}} + \frac{\left(d - \frac{r_o}{r_m}\right)\left(r_m - \frac{r_o}{\sqrt{2}}\right)}{1 - \frac{r_o}{r_m}} \end{cases}, \quad R(d) = \begin{cases} r_i & d \le \frac{r_i}{r_m} \\ d r_m & \frac{r_i}{r_m} < d \le \frac{r_o}{r_m} \\ r_m \left[\frac{1 - \frac{r_o}{r_m}}{1-d}\right]^{\left(\frac{r_m}{r_o} + \frac{1}{2}\right)} & d > \frac{r_o}{r_m} \end{cases}.$$

Note this is only for the eastern sector of the computational grid, where $x_c > 0$ and $|y_c| < x_c$; the other sections are analogous [3].

Some of the quadrilateral cells in the physical domain are nearly triangular, with two adjacent edges nearly colinear. In spite of this, the wave-propagation algorithm with transverse solvers described below works quite robustly in general as discussed further in [3]. However, when there is also a large jump in material parameters at the interface and the grids are adaptively refined there can be some stability issues as discussed further below.

Once the mapping is defined, we proceed by rotating the normal and transverse momentum components q^2 and q^3 of the Euler equations in the computational grid by using the normal at the current edge of the mapped grid, $\hat{n} = (n_x, n_y)$,

$$\begin{bmatrix} q^2_{ph} \\ q^3_{ph} \end{bmatrix} = \begin{bmatrix} n_x & n_y \\ -n_y & n_x \end{bmatrix} \begin{bmatrix} q^2 \\ q^3 \end{bmatrix},$$

where q^2_{ph} and q^3_{ph} now point in the normal and transverse direction in the physical domain (mapped grid). Using these quantities, we solve the normal Riemann solver as usual to obtain the speeds and waves s^p_{ph} and $\mathcal{W}^p_{ph}$, and we rotate the waves back to the computational domain,

$$\begin{bmatrix} \mathcal{W}^2 \\ \mathcal{W}^3 \end{bmatrix} = \begin{bmatrix} n_x & -n_y \\ n_y & n_x \end{bmatrix} \begin{bmatrix} \mathcal{W}^2_{ph} \\ \mathcal{W}^3_{ph} \end{bmatrix}.$$

Finally, we scale the speeds s^p_{ph} by the edge scaling to obtain s^p and employ the capacity function (cell area scaling) into a modified version of the algorithm in Eq. 3.24 found on [25].

The transverse solvers will also be applied on the mapped grid, but this requires more careful consideration because of our treatment of interfaces with huge jumps in the Tammann EOS parameters. This will be explained in detail in the next subsection. In this work, we implemented the 2D axisymmetric model into the mapped grid of Figure 4.3. Although the mapping is two-dimensional and shows half circular inclusions interfaces, the axisymmetry along the x axis convert these interfaces into spherical shells. This mapped grid was selected because it could be used to model a skull in computational TBI experiments. Note the mapping allows an inner interface that could even be used to model the thickness of a skull. The code is set up so arbitrary mappings with other interface geometries can be implemented.

In Figure 4.4, we show a sample simulation of the pressure contours for the mapped grid at six different points in time. It only employs one interface along the outer circular inclusion shown in the grid of Figure 4.3. Once again the outer part of the circular inclusion is modeled as air and the inner material as water using the same set of parameters as Figure 4.2. This figure also shows AMR in action with 4 levels of refinement, and it is also possible to add gauges to observe the pressure as a

function of time at any given point in the grid. AMR does not need many additional considerations in terms of the mapped grid since it works on the computational domain, which is still Cartesian. However, it is worth mentioning that the region around the interface is refined to the highest level from the beginning of the simulation. This is to avoid instabilities caused by employing AMR along an interface with huge jumps in the parameters while using a mapped grid with almost triangular grid cells (see Figure 4.3). If any of the conditions is relaxed, i.e. we use a smaller jump in the parameters or use a less severe mapped grid as in Figure 4.2, this initial refinement along the interface is no longer required to avoid instabilities.

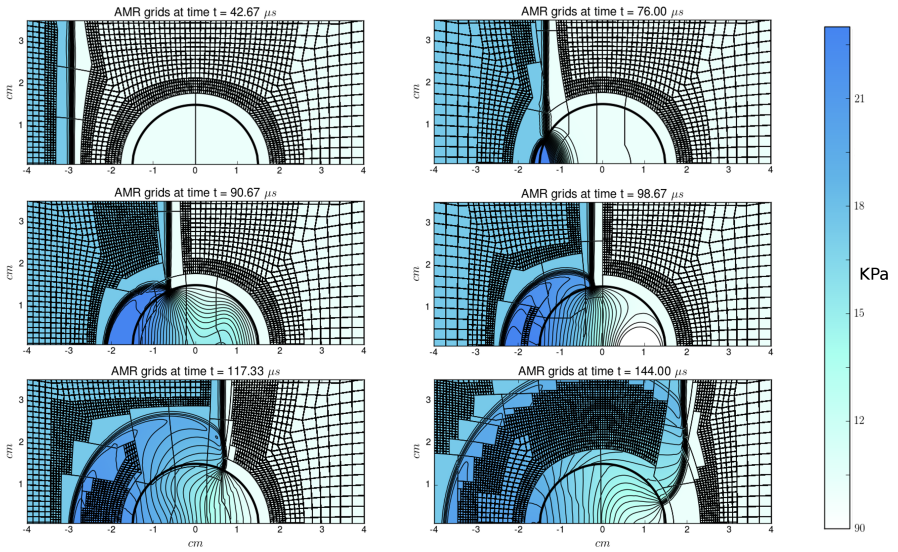
AMR grids at time t = 42.67 μs
AMR grids at time t = 76.00 μs
AMR grids at time t = 90.67 μs
AMR grids at time t = 98.67 μs
AMR grids at time t = 117.33 μs
AMR grids at time t = 144.00 μs
cm
KPa
21
18
15
12
90

Fig. 4.4: Pressure contour plots of axisymmetric simulation on a mapped grid with a circular inclusion at six different times points $t = 42.67, 76, 90.67, 98.67, 117.33, 144\ \mu s$, using four levels of AMR. The plot is analogous to that of Figure 4.2; however, in this figure the interface separating air and water is circular, which models a spherical water interface. Also note, the region around the interface is refined from the beginning to avoid instabilities when using AMR around corners in the mapped grid.

4.2. Transverse Riemann solver in a mapped grid. A transverse solver for a Cartesian grid was implemented in [9]. In this section, we show the extension of this transverse Riemann solver for a mapped grid. This solver takes the results of a normal Riemann solver and splits it into components moving in the transverse direction. As mentioned in [9], a special transverse solver needs to be developed due to instabilities at the interface. This is based on the solver for acoustics in a heterogeneous media that is described in Section 21.5 of [25].

We recall the basic idea of a transverse solver for a constant coefficient linear hyperbolic system of equations $q_t + Aq_x + Bq_y = 0$, the jump in normal flux between adjacent cells, $\mathcal{A}\Delta Q_{i-1/2} = \mathcal{A}(Q_{i,j} - Q_{i-1,j})$, is split via the normal Riemann solver into left-going and right-going "fluctuations" $\mathcal{A}^-\Delta Q_{i-1/2}$ and $\mathcal{A}^+\Delta Q_{i-1/2}$. Each fluctuation $\mathcal{A}^+\Delta Q_{i-1/2}$, is then further split into down-going and up-going components $\mathcal{B}^-\mathcal{A}^+\Delta Q_{i-1/2}$ and $\mathcal{B}^+\mathcal{A}^+\Delta Q_{i-1/2}$, based on the matrices B^+ and B^-.

In the case of variable coefficients or nonlinear problems, the general notation $\mathcal{B}^-\mathcal{A}^+\Delta Q_{i-1/2}$ and $\mathcal{B}^+\mathcal{A}^+\Delta Q_{i-1/2}$ is used for these two vectors. For variable coefficient acoustics, as described in [25], the up-going fluctuation from the transverse splitting is based on eigenvectors of B_{ij} and $B_{i,j+1}$, while the down-going fluctuation is based on eigenvectors of B_{ij} and $B_{i,j-1}$.

At the interface with an almost incompressible liquid, it is difficult to figure out an accurate and stable implementation of the transverse Riemann problem. This is because Euler equations, with a big jump in the parameters at the interface, are extremely sensitive to instabilities. Our first approach was to expand the normal wave as a function of linearized eigenvectors corresponding to the transverse grid cells [25] of the Euler equations. However, this approach resulted in instabilities at the interface. In order to work around this issue, we will follow the same approach as [9] and derive an approximate transverse Riemann solver based on acoustic equations, which capture the acoustic waves while avoiding instabilities.

In this interface, we will mostly be concerned with the two acoustic waves. In order to derive it, let $\hat{n} = (n_x, n_y)$ be the transverse unitary normal vector and linearize the acoustic equations around ρ_0, u_0 and v_0, with u_0 and v_0 the velocity in the x and y direction respectively [25]. In terms of the density and momentum,

$$\begin{bmatrix} \rho \\ \rho u \\ \rho v \end{bmatrix}_t + \underbrace{\begin{bmatrix} 0 & n_x & n_y \\ n_x c^2 & 0 & 0 \\ n_y c^2 & 0 & 0 \end{bmatrix}}_{\tilde{B}(Q)} \begin{bmatrix} \rho \\ \rho u \\ \rho v \end{bmatrix}_{\hat{n}} = 0, \tag{4.1}$$

where the derivative is taken in the normal direction $\hat{n}$, c is the sound speed and $\tilde{B}(Q)$ can be understood as a lower dimensional approximation of the transverse Jacobian $g'(Q_0)$ for the Euler equations. Note we assumed $u_0 = 0$, which is equivalent to move into a Lagrangian frame of reference.

As we might have different materials and sound speeds in the cell above or below, we calculate the eigenvectors and evaluate them according to their location. The matrix of eigenvectors is

$$R = \begin{bmatrix} 1 & 1 & 0 \\ n_x c_U & -n_x c_D & -n_y \\ n_y c_U & -n_y c_D & n_x \end{bmatrix},$$

where the sound speeds c_U and $-c_D$ are the eigenvalues corresponding to the first two column eigenvectors, v_u and v_d. The eigenvalue for the third one v_0 is 0. The subindex u and d refer to cells $(i, j+1)$ and (i, j) when computing $\mathcal{B}^+\mathcal{A}^+\Delta Q_{i-1/2,j}$ and to cells (i, j) and $(i, j-1)$ when computing $\mathcal{B}^-\mathcal{A}^+\Delta Q_{i-1/2,j}$.

The up-going and down-going fluctuations for $\mathcal{A}^+\Delta Q_{i-1/2,j}$ are obtained by expanding the fluctuation in terms of these eigenvectors or waves, $\mathcal{A}^+\Delta Q_{i-1/2,j} = \alpha_U v_U + \alpha_D v_D + \alpha_0 v_0$, so we need to solve $R\alpha = \mathcal{A}^+\Delta Q_{i-1/2,j}$, which yields

$$\begin{aligned} \alpha_U &= \frac{1}{c_U + c_D}\left(c_D \mathcal{A}_1^+ + n_x \mathcal{A}_2^+ + n_y \mathcal{A}_3^+\right), \\ \alpha_D &= \frac{1}{c_U + c_D}\left(c_U \mathcal{A}_1^+ - n_x \mathcal{A}_2^+ - n_y \mathcal{A}_3^+\right), \end{aligned}$$

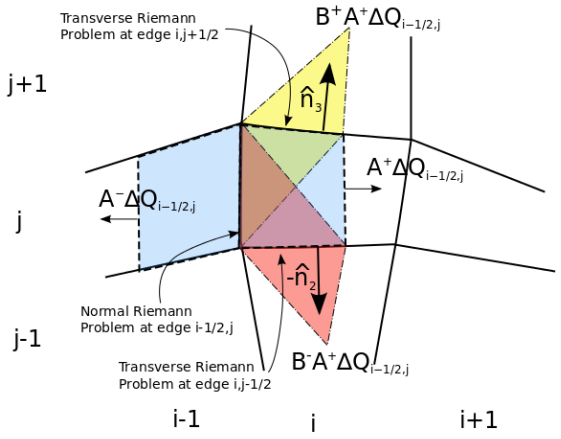

Fig. 4.5: Transverse solvers diagram in physical grid cells after applying the mapping. The left-going and right going fluctuations of the normal Riemann problem at the edge between grid cells $(i-1,j)$ and (i,j) is shown. The right-going fluctuation $\mathcal{A}^+\Delta Q_{i-1/2,j}$ is decomposed into the up-going fluctuation $\mathcal{B}^+\mathcal{A}^+\Delta Q_{i-1/2,j}$ and the down-going fluctuation $\mathcal{B}^-\mathcal{A}^+\Delta Q_{i-1/2,j}$ by employing transverse Riemann solvers in the computational grid. This is an extension of the transverse solvers implemented in [9] into mapped grids.

and α_0 is not relevant since it corresponds to the zero eigenvalue. Note that the required fluctuation $\mathcal{A}^+\Delta Q_{i-1/2,j}$ for the Euler equations is a four-dimensional vector with fluctuations in density, normal momentum, transverse momentum, and energy. As we are only interested in the acoustic waves, we will assume the fluctuations in energy are negligible, so we define the acoustic part of the fluctuation as the first second and third entry of the 4 dimensional vector, i.e. $\mathcal{A}^+_{ac}\Delta Q_{i-1/2,j} = [\mathcal{A}^+_1, \mathcal{A}^+_2, \mathcal{A}^+_3]$.

The up-going and down-going acoustic fluctuations are given by the velocity times the waves,

$$\mathcal{B}^+_{ac}\mathcal{A}^+\Delta Q_{i-1/2,j} = c_U \alpha_U v_U,$$
$$\mathcal{B}^-_{ac}\mathcal{A}^+\Delta Q_{i-1/2,j} = -c_D \alpha_D v_D.$$

We will need to solve two of these transverse solvers for the Euler equations as shown in the grid in Figure 4.5. We will only consider the up-going fluctuation of the transverse solver at $(i, j+1/2)$ and the down-going fluctuation of the solver at $i, j-1/2$. This yields the full fluctuations as

$$\mathcal{B}^+\mathcal{A}^+\Delta Q_{i-1/2,j} = \frac{c_3\left(c_2\mathcal{A}^+_1 + n_{3x}\mathcal{A}^+_2 + n_{3y}\mathcal{A}^+_3\right)}{c_3+c_2}\begin{bmatrix}1\\ n_{3x}c_3\\ n_{3y}c_3\\ 0\end{bmatrix},$$

$$\mathcal{B}^-\mathcal{A}^+\Delta Q_{i-1/2,j} = \frac{-c_1\left(c_2\mathcal{A}^+_1 - n_{2x}\mathcal{A}^+_2 - n_{2y}\mathcal{A}^+_3\right)}{c_1+c_2}\begin{bmatrix}1\\ -n_{2x}c_1\\ -n_{2y}c_1\\ 0\end{bmatrix},$$

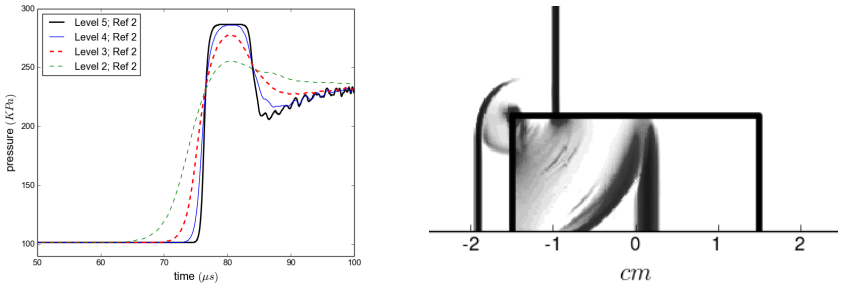

Fig. 4.6: In the first plot, we show a convergence study at a gauge at (-1cm,0). The curves shown are for four different AMR levels of refinement up to level 5, where each level doubles the resolution of the previous one. Oscillations are clearly seen in level 5 refinement. The second plot shows a schlieren plot for the pressure where one can appreciate the oscillations produced at the corner of the interface.

where c_1, c_2 and c_3 are the speeds of sound in cells $(i, j-1)$, (i, j) and $(i, j+1)$ respectively, the normals $\hat{n}_3$ and $\hat{n}_2$ are the normals to the upper edge and the lower edge, as shown in Figure 4.5, and the non-acoustic fluctuations were neglected. The sound speeds are calculated with the pressure, density and the parameters of the Tammann EOS in the respective cell with $c = \sqrt{\gamma \frac{p+p_\infty}{\rho}}$. This is repeated analogously for the left going fluctuation $\mathcal{A}^- \Delta Q_{i-1/2,j}$ of the normal Riemann problem. These transverse Riemann solvers were also implemented in the simulations shown in Figure 4.4.

4.3. Transmission based limiters. When the mesh is refined heavily by AMR, high-frequency unphysical oscillations appear in the water. Their wavelength scales with the mesh resolution, and they are hard to observe in the coarser grids due to numerical diffusion. These oscillations originate in the corner of the interface and they do not dissipate. This is caused by small errors produced by the Riemann solvers at the interface; these errors propagate in the normal and transverse direction. In the corner grid cell, these errors occur once when sweeping the solver on the grid horizontally and once again when sweeping vertically, producing oscillations. A sample of this phenomena can be observed in Figure 4.6, where we show the convergence study for a pressure gauge at (-1cm,0) and a schlieren plot of the pressure that shows the oscillations being produced at the corner of the interface. The convergence will be further studied in Section 5.

This issue can be improved by adjusting how the waves at the interface are limited. The limited waves from Eq. 3.25 are given by

$$\widetilde{\mathcal{W}}^p_{i\pm1/2} = \phi(\theta)^p_{i\pm1/2} \mathcal{W}^p_{i\pm1/2},$$

where $\phi(\theta)$ is the flux-limiter function [25] and θ is a measurement of the smoothness of the function. There are several ways to choose the θ parameter to limit the waves coming out of the edges at $i - 1/2$. For a linear problem with two waves, where the 1-waves propagate to the left and the 2-waves to the right (like acoustics), we can measure the smoothness θ by comparing the magnitude of adjacent waves. The corresponding θ parameters can be obtained as $\theta^1_{i-1/2} = \|\mathcal{W}^1_{i+1/2}\|/\|\mathcal{W}^1_{i-1/2}\|$ and $\theta^2_{i-1/2} = \|\mathcal{W}^2_{i-3/2}\|/\|\mathcal{W}^2_{i-1/2}\|$, see [25]. In the case of nonlinear equations, the ap-

proach is similar; however, the eigenvectors of adjacent waves are no longer co-linear in phase space across adjacent cells, so we need to do a projection into the corresponding eigenvectors. For the nonlinear case, the θ parameter is given by $\theta^1_{i-1/2} = (\mathcal{W}^1_{i+1/2}\cdot\mathcal{W}^1_{i-1/2})/(\mathcal{W}^1_{i-1/2}\cdot\mathcal{W}^1_{i-1/2})$ and $\theta^2_{i-1/2} = (\mathcal{W}^2_{i-3/2}\cdot\mathcal{W}^2_{i-1/2})/(\mathcal{W}^2_{i-1/2}\cdot\mathcal{W}^2_{i-1/2})$, see [25]. The diagrams in Figure 4.7 give some visual intuition into which waves we are comparing. This is the standard implementation in Clawpack [5].

In the case where there is a big jump in the parameters across an interface, the eigenvectors of a wave on different sides of the interface are significantly different. In this case, it is more appropriate to separate one of the adjacent waves into its transmitted and reflected component, as if it actually had crossed the interface, and use the transmitted wave to limit the other adjacent wave. For instance assume the interface is at the edge $i-1/2$ shown in Figure 4.7, the original limiter compares the projection of $W^1_{i+1/2}$ (into the corresponding eigenvector at $i-1$) with $W^1_{i-1/2}$ to limit $W^1_{i-1/2}$. However, if the interface has a big jump in the parameters, it is better to separate $W^1_{i+1/2}$ into its reflected and transmitted components and compare the transmitted component of the wave $T^1_{i-1/2}$ with $W^1_{i-1/2}$ to limit $W^1_{i-1/2}$. These type of limiters are called transmission based limiters, originally developed in [13] for acoustics equations in heteregeneous media. In this case, the θ parameters are given by

$$\theta^1_{i-1/2} = \frac{\|\mathcal{T}^1_{i-1/2}\|}{\|\mathcal{W}^1_{i-1/2}\|} \quad \theta^2_{i-1/2} = \frac{\|\mathcal{T}^2_{i-1/2}\|}{\|\mathcal{W}^2_{i-1/2}\|}, \tag{4.2}$$

where the transmitted waves $\mathcal{T}^{(1,2)}_{i-1/2}$ are as shown in Figure 4.7 correspondingly. This requires calculating the transmitted waves, which might follow different procedures depending on the equations we are using.

In this section, we extend the methods in [13] for acoustic equations to limit the acoustic waves in Euler equations. In order to do so, lets recall that we can rewrite the one-dimensional acoustic equations in terms of the density and the momentum [9, 25],

$$\begin{bmatrix} \rho \\ \rho u \end{bmatrix}_t + \begin{bmatrix} 0 & 1 \\ c^2 & 0 \end{bmatrix} \begin{bmatrix} \rho \\ \rho u \end{bmatrix}_x = 0, \tag{4.3}$$

where c is the sound speed, the eigenvalues of the system at a cell interface are the left and right sound speeds, $\lambda_{1,2} = -c_{i-1}, c_i$, and the corresponding eigenvectors $r^1_{i-1} = [1, -c_{i-1}]$ and $r^2_i = [1, c_i]$. As we assume different materials accross the interface $c_{i-1} \neq c_i$. Following the first diagram of Figure 4.7 and Eqs. 4.2, in order to calculate $\theta^1_{i-1/2}$, we need to know $\mathcal{T}^1_{i-1/2}$, which is the transmitted wave from wave $\mathcal{W}^1_{i+1/2}$ coming from cell i to cell $i-1$. In order to do so, we first write the wave $\mathcal{W}^1_{i+1/2}$ in terms of the corresponding eigenvector $\mathcal{W}^1_{i+1/2} = \alpha^1_{i+1/2} r^1_i$, which we already know from solving the Riemann problem, see [25]. Then we decompose it into the eigenvectors of the corresponding two cells to obtain the transmitted and reflected contributions,

$$\alpha^1_{i+1/2} \begin{bmatrix} 1 \\ -c_i \end{bmatrix} = \beta^1_{i+1/2} \begin{bmatrix} 1 \\ -c_{i-1} \end{bmatrix} + \beta^2_{i+1/2} \begin{bmatrix} 1 \\ c_i \end{bmatrix}.$$

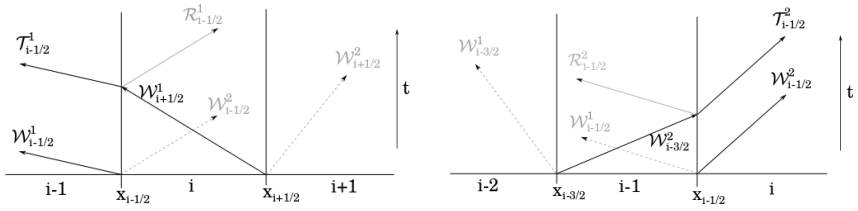

Fig. 4.7: Two diagrams are shown to illustrate the waves being compared in the different kind of limiters at the edge $i-1/2$, between grid cells $i-1$ and i. The first diagram shows the waves that are involved in determining $\theta^1_{i-1/2}$ for the limiting behavior of $\mathcal{W}^1_{i-1/2}$. The second one shows the waves involved in determining $\theta^2_{i-1/2}$ for the limiting behavior of $\mathcal{W}^2_{i-1/2}$. The notation is $\mathcal{T}$ for transmitted waves and $\mathcal{R}$ for reflected ones.

This yields two equations with two unknowns, so we can solve for the $\beta^1_{i+1/2}$,

$$\beta^1_{i+1/2} = \alpha^1_{i+1/2}\frac{2c_i}{c_{i-1}+c_i}.$$

This quantity multiplied by the eigenvector r^1_{i-1} corresponds to the transmitted wave. With this information, and using that $\mathcal{W}^1_{i-1/2} = \alpha^1_{i-1/2}r^1_{i-1}$, we can now calculate the θ parameter,

$$\theta^1_{i-1/2} = \frac{\|\mathcal{T}^1_{i-1/2}\|}{\|\mathcal{W}^1_{i-1/2}\|} = \frac{\alpha^1_{i+1/2}}{\alpha^1_{i-1/2}}\left(\frac{2c_i}{c_{i-1}+c_i}\right),$$
$$\theta^2_{i-1/2} = \frac{\|\mathcal{T}^2_{i-1/2}\|}{\|\mathcal{W}^2_{i-1/2}\|} = \frac{\alpha^2_{i-3/2}}{\alpha^2_{i-1/2}}\left(\frac{2c_{i-1}}{c_i+c_{i-1}}\right),$$

where $\theta^2_{i-1/2}$ is calculated in the same manner by following the second diagram from Figure 4.7. The sound speeds can be obtained from the Tammann EOS by using Eqs. 3.2 and 3.22. Also note the limiters work on the waves in the computational domain, so it is not necessary to do any additional adjustments when using a mapped grid.

These limiters greatly improve the observed oscillations as shown in the first plot of Figure 5.1 where the level 5 refinement no longer shows significant oscillations. Note these limiters are approximate since we are using the acoustic equations rewritten in terms of density and momentum to limit the Euler equations, and they don't fully suppress the oscillations in higher refinement levels as we will see in the next Section.

5. Verification. A verification study for the one-dimensional case was performed in a previous work [9]. In that work, we verified that the finite volume methods coupled with the hybrid Riemann HLLC-exact Riemann solver for the Euler equations with a Tammann EOS converge to the correct solution for a simple model problem. However, the exact analytic solutions of Riemann problems for Euler equations are only available in one dimension, so we restricted our verification to a one-dimensional test. Nonetheless, as the Riemann problem is still the key ingredient of higher-dimensional numerical methods, the analysis from [9] is still relevant for the two-dimensional extension of the algorithm.

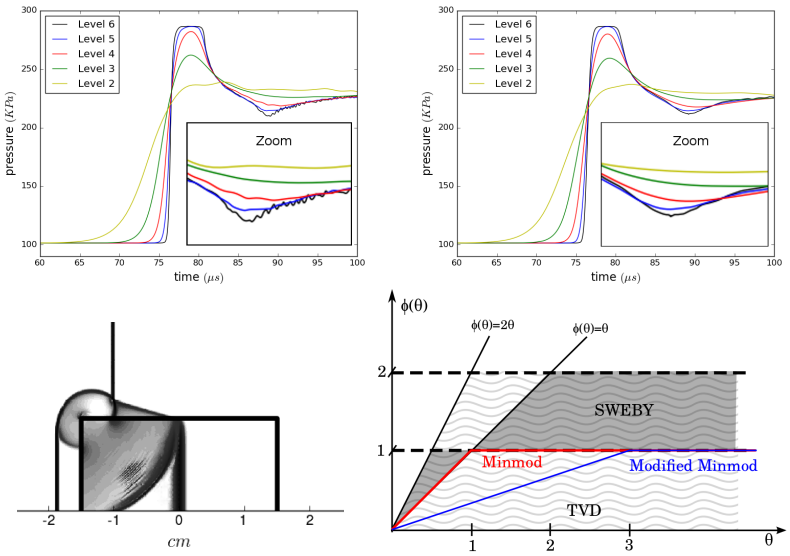

Fig. 5.1: The first two plots show the convergence tests at a gauge in (-1cm,0) for the two dimensional axisymmetric model with AMR on a Cartesian grid. The curves are shown for different levels of refinement allowed in AMR, where each level doubles the resolution of the previous one. In the first plot one can appreciate numerical high frequency oscillations in the finer grids; however, this are almost fully supressed in the second figure by using a more diffusive limiter, the modified minmod limiter. The third plot shows a schlieren plot of the pressure with level 6 refinement when using the original minmod limiter. It shows high-frequency oscillations propagating from the corner that do not dissipate. The fourth plot shows the TVD region (wavy lines) and the Sweby region (shaded) [25] as well as the corresponding minmod and modified minmod limiter.

In addition to the verification study presented in [9], in this work we will provide a convergence test for the two-dimensional axisymmetric model. As there are no exact solutions for the two-dimensional equations, the convergence test only shows the numerical algorithm converges to a solution as the mesh is refined. The convergence tests were performed using several gauges for the Cartesian grid simulations of Figure 4.2. In the first plot in Figure 5.1, we show the convergence test for the gauge at (-1cm,0). Note the appearance of high-frequency oscillations in the most refined level (level 6) even after applying the transmission-based limiters. The plot at the bottom-left of Figure 5.1 shows these oscillations for the finest grid in a schlieren pressure plot. The origin of this oscillations is the same as before.

These oscillations can be suppressed by adding some numerical viscosity to the water material. This is not entirely unphysical since the water is a viscous media. In order to do so, we implement a new limiter for the water grid cells, which we refer to as modified minmod. The original minmod limiter uses the flux-limiter function $\phi(\theta) = \text{minmod}(1, \theta)$ [25]. The minmod limiter is the most dissipative second-order total variation diminishing (TVD) limiter. This is shown in the flux-limiter function plot at the bottom-right of Figure 5.1. The region covered in wavy lines is the region

where the limiter can be TVD, and the shaded region shows the Sweby region where limiter can be second-order accurate; the corresponding flux-limiter function for the minmod limiter is shown too. In order to add more numerical viscosity, we use a modified minmod limiter $\phi(\theta) = \text{minmod}(1, \theta/3)$. Although we lose second order accuracy for the Euler Equations, this limiter still provides physical solutions due to water viscosity. The scaling factor within the flux-limiter function $(1/3)$ was chosen to be as close to 1 as possible to keep as much overlap with the Sweby region as possible while also supressing the oscillations; this parameter can be easily adjusted in the code, which is available in [7]. The resulting convergence study after applying the modified minmod limiter can be appreciated in the second plot of Figure 5.1, where we can observe the oscillations were suppressed and that our method converges. Analogous results were obtained for the other gauges.

6. Discussion. We developed a two-dimensional axisymmetric shock-capturing high-resolution numerical model to study shock wave dynamics when crossing a fixed interface between a compressible fluid (air) and an almost incompressible material (water). These methods have been designed to complement TBI and other biomedical experiments performed in a shock tube. The common setup in these experiments consists of a shock wave traveling through air and impacting a plastic container. The container is usually very thin, and it is often filled with an aqueous solution where the biological sample is placed. In our computational simulations, the container is modeled as an interface fixed in space. The aim of these methods and simulations is to provide experimentalists measurements of relevant variables inside the container, like pressure, that would otherwise be very difficult to obtain experimentally. This can help us understand better the on-going physical dynamics that experimental samples in specifc experiments undergo and explain possible damage mechanisms. It should be noted the methods developed here can be extended to other scenarios.

We first provided the one-dimensional methods employed in detail and their implementation into Clawpack [5]. In Appendix A we show that there is not a significant difference between the transmitted shock wave when removing the thin plastic interface separating air and water. Furthermore, we observed an amplification and elongation of the shock wave. This effect is accounted for by the different material compressibility. The amplitude of the initial pressure wave in the air increased in 54% when measured in the water. This amplification effect was highly relevant in the injury mechanisms studied in [9], and it generally occurs when passing from air to water or a solid material.

The methods were extended to two dimensions and implemented on a mapped grid, which allows more complicated interface geometries as long as the mapping is provided. We provided as a proof of concept a circular inclusion mapping, which maps the rectangular interface into a circular one. In the axisymmetric case, this mapping models a spherical interface. In addition, the algorithms were adapted to work with AMR to increase resolution and efficiency of the code. Additional mathematical work has to be performed to improve the accuracy and stability of the numerical method. Transverse Riemann solvers for the mapped grid were developed to improve the accuracy. Transmission-based limiters and the minmod modified limiter were implemented at the interface and in the water to suppress numerical oscillations at heavily refined AMR patches. A more primitive version of these methods was already employed in a specific mild TBI application [9], and we expect they can be extended and used in new applications. The three-dimensional model with a spherical shell inclusion could be specifically useful in TBI applications to model an idealized skull

of a mouse inside the shock tube or a human head exposed to a shock, a problem of much interest to the TBI community as shown by some previous studies [1, 18, 23, 31, 36, 40, 41, 42, 43, 44, 47, 49] among others. The code where all these methods are implemented is available with a BSD license [7].

Appendix A. One dimensional computational experiments. In this section, we simulate the one-dimensional Euler equations 3.4 with the numerical methods from Section 3. We explore the question of whether a thin plastic interface separating gas and liquid in a shock tube experiment can be ignored in computational experiments, specifically whether the magnitude of the shock wave transmitted from the gas to the liquid is insensitive to the intervening layer of plastic. In the laboratory experiments that motivated this work, the walls of the plastic transwell container are thin relative to the dimensions of the interior, and the computations presented in [9] were simplified by omitting the plastic layer entirely. Here we justify that approximation by considering a simple one-dimensional model of a shock wave passing through layers of air-plastic-water. This will provide insight on the behavior of the shock wave; it will show what parameters are the most relevant, and it will show that it is not necessary to include the thin plastic interface in the computational model. We will begin with a one-dimensional air-plastic-water interface using Euler equations, and then we compare these results to the simpler one-dimensional air-water interface, omitting the plastic layer. We will further verify our results with an analytic calculation for a thin interface in linear acoustics. A preliminary version of this study can also be found in the conference proceedings [8].

A.1. Air-plastic-water interface. We begin by studying an air-plastic-water interface with Euler equations 2.1 in one dimension,

$$\frac{\partial}{\partial t}\begin{bmatrix}\rho\\ \rho u\\ E\end{bmatrix}+\frac{\partial}{\partial x}\begin{bmatrix}\rho u\\ \rho u^2+p\\ u(E+p)\end{bmatrix}=0. \tag{A.1}$$

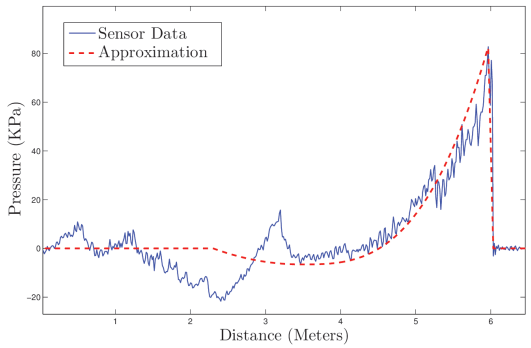

Fig. A.1: The shock wave form obtained from a sensor inside a shock tube is shown as the solid thin line. The coarse approximation to be used as an initial condition in our simulation is shown with a dashed line. An average speed of sound of $c = 344$ m/s is assumed. These figure was obtained from [9].

The first step is to input the right initial conditions into our simulation. The

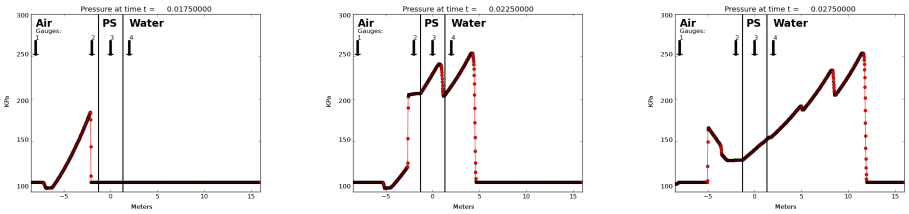

(a) (b) (c)

Fig. A.2: Shock wave crossing the air-plastic-water interface at different times. The arrows indicate the position of the 4 gauges that measure the pressure as a function of time. The gauges are numbered from left to right, and the plastic interface width for this case is 2.6m

actual form of the initial shock wave traveling through the shock tube was obtained experimentally; the amplitude can be varied in the shock tube and in our computational simulations. The sensor outputs pressure amplitude as a function of time. Assuming an average speed of sound in air, it can be converted to a function of distance as shown in Figure A.1. The shape can be broadly approximated by an idealized shock wave (dashed line in Figure A.1). This approximated shape of the shock wave is introduced as the initial condition in the simulation, where a scaling factor is used to scale the amplitude; however, this is not a trivial procedure since we must input the density, momentum, and energy, and we only have the pressure. Using the isentropic EOS, the ideal gas EOS and the expression for the speed of sound, an educated guess for the initial condition in terms of the pressure is given far away from the transwell. This initial condition is then modified until we obtain the desired amplitude and shape of the shock wave front. The resulting shape of the shock wave before hitting the interface can be seen in Figure A.2(a), where the scaling factor, in this case, was chosen arbitrarily. The pressure is measured in KPa with an ambient base pressure of 1ATM = 101.325KPa. The same procedure was used for the two-dimensional simulations.

The one-dimensional equations with the pair of interfaces are solved using the methods mentioned in Section 3. The different materials are modeled using different parameters for the Tammann EOS, see Section 2.1. The choice of parameters is shown in Table 2.1.

The solution of the shock wave crossing the interfaces between air, plastic, and water at different times is shown in Figure A.2. It can be observed that every time the shock wave hits an interface, part of the wave is reflected and part of it is transmitted. This effect can occur multiple times depending on how the interfaces are set up. We can also observe that the amplitude of the shock wave increases as it passes from air to plastic and decreases when passing from plastic to water. This effect is due to the continuity of pressure and the change in compressibility. In order to keep the pressure at the interface continuous, the transmitted wave amplitude has to be the same as the sum of the incident wave and the reflected wave. When the compressibility is very high in the adjacent material, the interface will behave similarly to a solid wall. In this case, since the reflected wave will have an amplitude almost equal to the incident wave, the transmitted wave could have an amplitude almost twice as big as that of

Width (m)	Initial(KPa)	Gauge 2 (KPa)	Gauge 3 (KPa)	Gauge 4 (KPa)
2.6	184.06	247.76	305.88	258.24
1.4	184.06	207.53	298.19	259.71
0.6	184.06	187.72	283.72	274.90
0.2	184.06	183.31	282.34	280.18
0.1	184.06	183.31	284.29	283.55
0.0	184.06	184.40	-	284.26

Table A.1: The maximum amplitude measured at three pressure gauges for different widths of the plastic interface. The initial shock wave is the same for all cases, and the gauge plots are placed before, inside and after the plastic interface as shown in Figure A.2. The last row corresponds to the air-water interface.

the incident wave. This explains why the pressure jump can increase or decrease when crossing an interface. Even for the one-dimensional case, we observe complex behavior due to interaction at the interface. These numerical simulations provide accurate insight in situations where simple intuition might be insufficient.

In Figure A.1, we show from experimental data the initial shock wave profile in the air before hitting any interface; however, we are interested in the shape and amplitude of the shock wave in the water. In order to do so, we first need to know how important the plastic interface is in our model. Computationally, the plastic interface is hard to model because the width of the plastic is very small (mm) in comparison to the characteristic length of the experiment (length of the transwell [9]). The following experiment explores how the width of the plastic interface affects the shock wave profile. Additionally, we show an accurate model can be obtained even when completely ignoring the plastic interface.

The maximum amplitude of the pressure profile was measured at gauges $2, 3$ and 4 of Figure A.2 for different widths of the plastic interface. The plastic is always assumed to be centered at $x = 0$. The results are presented in Table A.1. In Figure A.3, the full pressure profiles as a function of time are shown at the three gauges for three of the plastic widths shown in Table A.1.

The results in Table A.1 and Figure A.3 show the maximum amplitude at gauge 2 is reduced as the plastic width is decreased. Not surprisingly, this is a consequence of having less interference with the reflected shock wave, since the gauge is farther away from the interface as the plastic width is reduced. This effect is clearly shown in Figures A.3a, A.3d, A.3g. The maximum amplitude at gauge 3 is somewhat diminished at first; however, it seems to be reaching a plateau around 280.0KPa. The behavior at gauge 3 is not trivial; the shock wave bounces back and forth several times, interfering with itself constantly. In Figures A.3b, A.3e, A.3h, we can see the interference becomes so fast that the pressure profile in the plastic seems to converge to a shock wave shape as the plastic width is reduced. At gauge 4, we can observe the interference between the set of transmitted shock waves generated by the back and forth reflections within the plastic interface. As the plastic width is reduced, the time elapsed between the transmitted shock waves is reduced and the interference increased. Nonetheless, when the plastic width is very small, the interference becomes so fast that the pressure profile seems to converge again to a shock wave shape, as shown in Figures A.3c, A.3f, A.3i. Furthermore, note the difference in the shock wave shape in Figures A.3h, A.3i is almost unnoticeable. It almost seems like

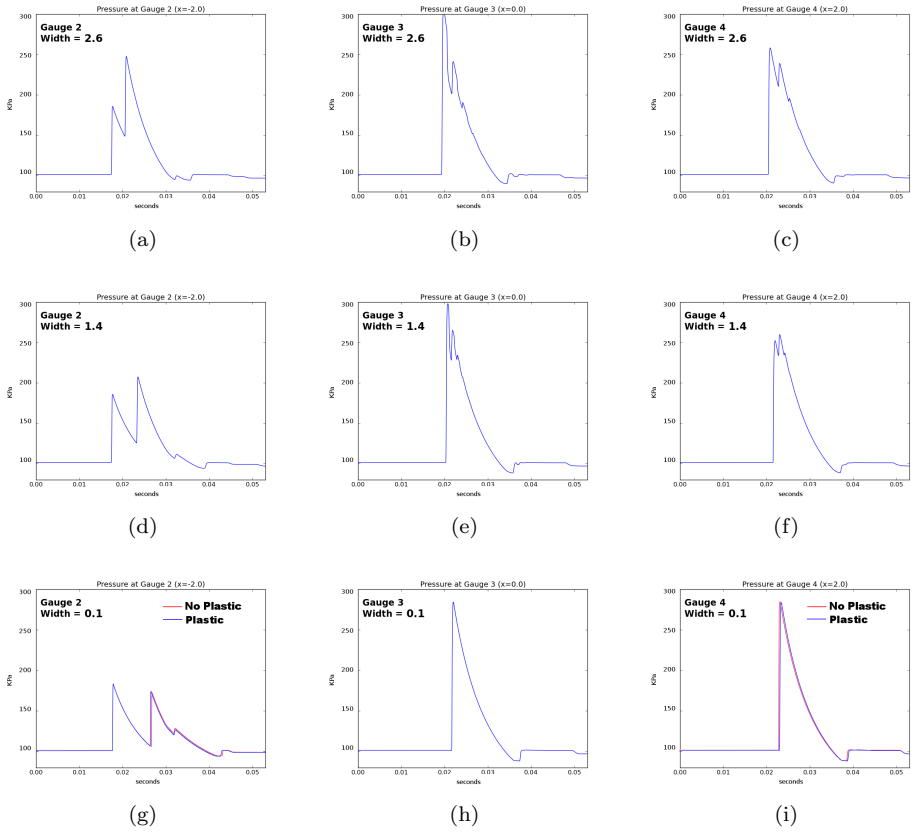

Fig. A.3: Pressure (KPa) gauge plots as a function of time (seconds). Each row of figures shows the three gauge plots for three different widths (2.6m, 1.4m and 0.1m) of the plastic interface, as shown in Table A.1. The plots (g) and (i) for gauge 2 and 4 also show the pressure gauge plots when there is no plastic interface at all; the difference is almost unnoticeable. Also note the red line in Figure A.3(g) is completely overlapped by the blue line before the reflected shock appears; this is because the solutions between thin plastic and no plastic are exactly the same before interacting with the interface.

the shock wave is only crossing one interface instead of two. This motivates the next experiment.

A.2. Air-water interface. In reality, the plastic is so thin that is really unnoticeable on larger scales. Furthermore, as the plastic is almost an incompressible medium, one should expect it would transfer the shock wave infinitely fast without energy loss. Therefore, instead of the triple material interface, now consider only an air-water interface. The result of this simulation is shown in Figure A.4. The gauge plots for gauge 2 and 4 are shown in Figures A.3g and A.3i, along with the thin plastic results. The maximum amplitude in each of these gauges is presented in the last row of Table A.1.

Comparing the air-water interface results against the ones for the smallest plastic

width in the air-plastic-water interface case, we can observe the percentage error in the maximum pressure amplitude of gauge 4 is of 0.38%. This is also obvious from the thin plastic and no plastic comparison in Figures (A.3g, A.3i). This result allowed us to simplify higher dimensional air-plastic-water interface problem to a simpler air-water interface in the work [9]. Nonetheless, the presence of the plastic is still modeled, since we force our interfaces to be fixed in space, just as a plastic container would force water to remain inside the container.

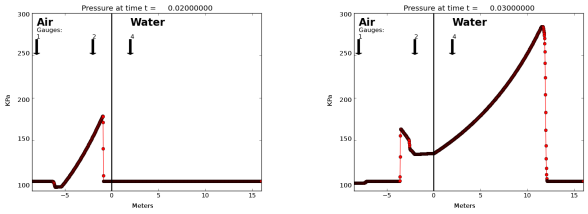

(a) (b)

Fig. A.4: Shock wave before and after crossing the air-water interface. The arrows indicate the position of the gauges that measure the pressure as a function of time. The gauges are the same as in Figure A.2. Gauge 3 was removed since there is no plastic layer in this case.

A.3. Air-Plastic-Water interface with linear acoustics. In order to further justify dropping the plastic layer, we consider the same situation of a thin intermediate layer for the case of linear acoustics. In this case, we can compute the exact solution of the transmitted pressure through the air-plastic-water interface as a function of the acoustic impedance of each material and the plastic width. This can be derived from the fact that an acoustic wave with incident pressure jump p_0 on the left of an interface between medium A (left) and B(right) produces a reflected and a transmitted wave with pressure jumps given by,

$$p_T = p_0 \frac{2Z_B}{Z_A + Z_B} \qquad p_R = p_0 \frac{Z_B - Z_A}{Z_A + Z_B},$$

where Z_k denotes the acoustic impedance of medium k. These relations can be easily derived from linear acoustics [25]. Now consider a one-dimensional air-plastic-water interface. With this setup, there will be an infinite number of reflections in the plastic layer. The N^{th} wave contribution to the transmitted wave in water is given by

$$p_T^N = \frac{2Z_w}{Z_w + Z_p} \left(\frac{Z_a - Z_p}{Z_a + Z_p} \right)^{N-1} \left(\frac{Z_w - Z_p}{Z_w + Z_p} \right)^{N-1} \frac{2Z_p}{Z_p + Z_a} p_0,$$

where Z_a, Z_p, and Z_w are the air, plastic and water impedances. Each transmitted wave increases the pressure behind the initial transmitted wave slightly and the asymptotic final amplitude of the transmitted wave is given by the sum of all these

contributions,

$$p_T^{total} = \sum_{N=1}^{\infty} p_T^N = \frac{4Z_w Z_p p_0}{(Z_w + Z_p)(Z_p + z_a)} \sum_{N=0}^{\infty} \left(\frac{(Z_a - Z_p)(Z_w - Z_p)}{(Z_a + Z_p)(Z_w + Z_p)} \right)^N.$$

Summing this geometric series yields

$$p_T^{total} = p_0 \frac{2Z_w}{Z_w + Z_a}.$$

When the plastic layer is very thin, this asymptotic value is quickly reached, and we note that it is exactly the same as if the plastic interface didn't exist. The transmission coefficient is the one computed directly from air into water. Note we assumed the pressure profile on the left was a constant p_0. However, this can be more complicated. It can have a decaying tail, in which case there will be interference from the tail in the reflected and transmitted waves. Nonetheless, assuming the plastic width is w_0, the time elapsed between two transmitted waves in the water interface is given by $\tau = 2w_0/c_p$, where c_p is the speed of sound in plastic. Therefore, as $w_0 \to 0$, the elapsed time $\tau \to 0$. As a consequence, the interference from the tail will also disappear and the plastic interface can be neglected without losing accuracy.

This calculation is an analytic result that shows that if the plastic interface is very thin in comparison to the experiment's characteristic length scales, the plastic interface can be neglected without losing much accuracy.

REFERENCES

[1] J. D. Anderson, *Modern compressible flow with historical perspective*, 2003.

[2] M. J. Berger and R. J. LeVeque, *Adaptive mesh refinement using wave-propagation algorithms for hyperbolic systems*, SIAM Journal on Numerical Analysis, 35 (1998), pp. 2298–2316.

[3] D. A. Calhoun, C. Helzel, and R. J. LeVeque, *Logically rectangular grids and finite volume methods for pdes in circular and spherical domains*, SIAM review, (2008), pp. 723–752.

[4] A. Chertock, S. Karni, and A. Kurganov, *Interface tracking method for compressible multifluids*, ESAIM: Mathematical Modelling and Numerical Analysis, 42 (2008), pp. 991–1019.

[5] Clawpack Development Team, *Clawpack software*, 2015. Version 5.2.2.

[6] C. Coisne, L. Dehouck, C. Faveeuw, Y. Delplace, F. Miller, C. Landry, C. Morissette, L. Fenart, R. Cecchelli, P. Tremblay, et al., *Mouse syngenic in vitro blood–brain barrier model: a new tool to examine inflammatory events in cerebral endothelium*, Laboratory investigation, 85 (2005), pp. 734–746.

[7] M. J. Del Razo and R. J. LeVeque, *Code and data to accompany this paper*. Github https://github.com/maojrs/Interface_Euler_AMR/, 2015.

[8] M. J. Del Razo and R. J. LeVeque, *Computational study of shock waves propagating through air-plastic-water interfaces*, Bulletin of the Brazilian Math. Society, HYP2014 conference proceedings (in press). (2015).

[9] M. J. Del Razo, Y. Morofuji, J. S. Meabon, B. R. Huber, E. R. Peskind, W. A. Banks, P. D. Mourad, R. J. LeVeque, and D. G. Cook, *Computational and in vitro studies of blast-induced blood-brain barrier disruption*, (2015, SIAM Journal on Scientific Computing (in press)).

[10] B. Einfeldt, *On godunov-type methods for gas dynamics*, SIAM Journal on Numerical Analysis, 25 (1988), pp. 294–318.

[11] K. Fagnan, R. J. LeVeque, and T. J. Matula, *Computational Models of Material Interfaces for the Study of Extracorporeal Shock Wave Therapy*, (2012), pp. 1–29.

[12] K. Fagnan, R. J. LeVeque, T. J. Matula, and B. MacConaghy, *High-resolution finite volume methods for extracorporeal shock wave therapy*, in Hyperbolic Problems: Theory, Numerics, Applications, Springer, 2008, pp. 503–510.
[13] T. R. Fogarty and R. J. LeVeque, *High-resolution finite-volume methods for acoustic waves in periodic and random media*, The Journal of the Acoustical Society of America, 106 (1999), pp. 17–28.
[14] S. K. Godunov, *A difference method for numerical calculation of discontinuous solutions of the equations of hydrodynamics*, Matematicheskii Sbornik, 89 (1959), pp. 271–306.
[15] J. Goeller, A. Wardlaw, D. Treichler, J. O'Bruba, and G. Weiss, *Investigation of cavitation as a possible damage mechanism in blast-induced traumatic brain injury*, Journal of neurotrauma, 29 (2012), pp. 1970–1981.
[16] L. E. Goldstein, A. M. Fisher, C. A. Tagge, X.-L. Zhang, L. Velisek, J. A. Sullivan, C. Upreti, J. M. Kracht, M. Ericsson, M. W. Wojnarowicz, et al., *Chronic traumatic encephalopathy in blast-exposed military veterans and a blast neurotrauma mouse model*, Science translational medicine, 4 (2012), pp. 134ra60–134ra60.
[17] R. K. Gupta and A. Przekwas, *Mathematical models of blast-induced tbi: current status, challenges, and prospects*, Frontiers in neurology, 4 (2013).
[18] J. Ho and S. Kleiven, *Dynamic response of the brain with vasculature: a three-dimensional computational study*, Journal of biomechanics, 40 (2007), pp. 3006–3012.
[19] X. Hu, N. Adams, and G. Iaccarino, *On the HLLC Riemann solver for interface interaction in compressible multi-fluid flow*, Journal of Computational Physics, 228 (2009), pp. 6572–6589.
[20] B. R. Huber, J. S. Meabon, T. J. Martin, P. D. Mourad, R. Bennett, B. C. Kraemer, I. Cernak, E. C. Petrie, M. J. Emery, E. R. Swenson, et al., *Blast exposure causes early and persistent aberrant phospho-and cleaved-tau expression in a murine model of mild blast-induced traumatic brain injury*, Journal of Alzheimer's disease, 37 (2013), pp. 309–323.
[21] C. D. Hue, S. Cao, S. F. Haider, K. V. Vo, G. B. Effgen, E. Vogel III, M. B. Panzer, C. R. Bass, D. F. Meaney, and B. Morrison III, *Blood-brain barrier dysfunction after primary blast injury in vitro*, Journal of neurotrauma, 30 (2013), pp. 1652–1663.
[22] M. Ivings, D. Causon, and E. Toro, *On riemann solvers for compressible liquids*, International Journal for Numerical Methods in Fluids, 28 (1998), pp. 395–418.
[23] S. Kleiven, *Predictors for traumatic brain injuries evaluated through accident reconstructions*, tech. report, SAE Technical Paper, 2007.
[24] R. J. LeVeque, *Wave propagation algorithms for multidimensional hyperbolic systems*, Journal of Computational Physics, 131 (1997), pp. 327–353.
[25] R. J. LeVeque, *Finite Volume Methods for Hyperbolic Problems*, Cambridge, 2002.
[26] ———, *Finite Difference Methods for Ordinary and Partial Differential Equations: Steady State and Time Dependent Problems*, Cambridge University Press, 2007.
[27] T. Liu, B. Khoo, and W. Xie, *Isentropic one-fluid modelling of unsteady cavitating flow*, Journal of Computational Physics, 201 (2004), pp. 80–108.
[28] T. Liu, B. Khoo, and K. Yeo, *Ghost fluid method for strong shock impacting on material interface*, Journal of Computational Physics, 190 (2003), pp. 651–681.
[29] H. F. Mark, *Encyclopedia of polymer science and technology, concise*, John Wiley & Sons, 2013.
[30] D. F. Moore, A. Jérusalem, M. Nyein, L. Noels, M. S. Jaffee, and R. A. Radovitzky, *Computational biologymodeling of primary blast effects on the central nervous system*, Neuroimage, 47 (2009), pp. T10–T20.
[31] W. C. Moss, M. J. King, and E. G. Blackman, *Skull flexure from blast waves: a mechanism for brain injury with implications for helmet design*, Physical review letters, 103 (2009), p. 108702.
[32] M. K. Nyein, A. M. Jason, L. Yu, C. M. Pita, J. D. Joannopoulos, D. F. Moore, and R. A. Radovitzky, *In silico investigation of intracranial blast mitigation with relevance to military traumatic brain injury*, Proceedings of the National Academy of Sciences, 107 (2010), pp. 20703–20708.
[33] M. B. Panzer, B. S. Myers, B. P. Capehart, and C. R. Bass, *Development of a finite element model for blast brain injury and the effects of csf cavitation*, Annals of biomedical engineering, 40 (2012), pp. 1530–1544.
[34] M. Pelanti and K.-M. Shyue, *A mixture-energy-consistent six-equation two-phase numerical model for fluids with interfaces, cavitation and evaporation waves*, Journal of Computational Physics, 259 (2014), pp. 331–357.
[35] A. Przekwas, M. Somayaji, and Z. Chen, *A mathematical model coupling neuroexcitation,*

astrocyte swelling and perfusion in mild tbi, in Int. State-of-the-Science Meeting on Non-Impact, Blast-Induced Mild Traumatic Brain Injury, VA Herndon, 2009.

[36] J. S. Ruan, T. B. Khalil, and A. I. King, *Finite element modeling of direct head impact*, tech. report, SAE Technical Paper, 1993.

[37] V. Rubovitch, M. Ten-Bosch, O. Zohar, C. R. Harrison, C. Tempel-Brami, E. Stein, B. J. Hoffer, C. D. Balaban, S. Schreiber, W.-T. Chiu, et al., *A mouse model of blast-induced mild traumatic brain injury*, Experimental neurology, 232 (2011), pp. 280–289.

[38] R. Saurel and O. Lemetayer, *A multiphase model for compressible flows with interfaces, shocks, detonation waves and cavitation*, Journal of Fluid Mechanics, 431 (2001), pp. 239–271.

[39] R. Saurel, F. Petitpas, and R. A. Berry, *Simple and efficient relaxation methods for interfaces separating compressible fluids, cavitating flows and shocks in multiphase mixtures*, Journal of Computational Physics, 228 (2009), pp. 1678–1712.

[40] D. I. Shreiber, A. C. Bain, and D. F. Meaney, *In vivo thresholds for mechanical injury to the blood-brain barrier*, tech. report, SAE Technical Paper, 1997.

[41] A. Sundaramurthy, A. Alai, S. Ganpule, A. Holmberg, E. Plougonven, and N. Chandra, *Blast-induced biomechanical loading of the rat: an experimental and anatomically accurate computational blast injury model*, Journal of neurotrauma, 29 (2012), pp. 2352–2364.

[42] E. G. Takhounts, R. H. Eppinger, J. Q. Campbell, R. E. Tannous, E. D. Power, and L. S. Shook, *On the development of the simon finite element head model*, tech. report, SAE Technical Paper, 2003.

[43] E. G. Takhounts, S. A. Ridella, V. Hasija, R. E. Tannous, J. Q. Campbell, D. Malone, K. Danelson, J. Stitzel, S. Rowson, and S. Duma, *Investigation of traumatic brain injuries using the next generation of simulated injury monitor (simon) finite element head model*, Stapp Car Crash J, 52 (2008), pp. 1–31.

[44] P. A. Taylor and C. C. Ford, *Simulation of blast-induced early-time intracranial wave physics leading to traumatic brain injury*, Journal of biomechanical engineering, 131 (2009), p. 061007.

[45] E. F. Toro, *Riemann Solvers and Numerical Methods for Fluid Dynamics*, Springer, 2008.

[46] H. Udaykumar, R. Mittal, and P. Rampunggoon, *Interface tracking finite volume method for complex solid–fluid interactions on fixed meshes*, Communications in numerical methods in engineering, 18 (2002), pp. 89–97.

[47] W. Wakeland and B. Goldstein, *A computer model of intracranial pressure dynamics during traumatic brain injury that explicitly models fluid flows and volumes*, in Intracranial Pressure and Brain Monitoring XII, Springer, 2005, pp. 321–326.

[48] C. Wang, H. Tang, and T. Liu, *An adaptive ghost fluid finite volume method for compressible gas–water simulations*, Journal of computational physics, 227 (2008), pp. 6385–6409.

[49] C. Zhou, T. Khalil, and A. I. King, *Viscoelastic response of the human brain to sagittal and lateral rotational acceleration by finite element analysis*, in Proceedings of the International Research Council on the Biomechanics of Injury conference, vol. 24, International Research Council on Biomechanics of Injury, 1997, pp. 35–48.

[50] M. Ziejewski, G. Karami, and A. Akhatov, *Selected biomechanical issues of brain injury caused by blasts*, Brain Inj. Prof, 4 (2007), pp. 10–15.